# Site-Specific Controller Design for Monopile Offshore Wind Turbines

Emil Smilden[a,b,*], Erin E. Bachynski[a,b], Asgeir J. Sørensen[a,b], Jørgen Amdahl[a,b]

[a] *Centre for Autonomous Marine Operations and Systems, Norwegian University of Science and Technology, Trondheim, Norway*
[b] *Department of Marine Technology, Norwegian University of Science and Technology, Trondheim, Norway*

**Abstract**

The fatigue life of offshore wind turbine (OWT) support structures is sensitive to variations in site-specific conditions such as the water depth and soil properties. Site condtions may vary significantly within a wind farm, and they may change throughout the lifetime of the OWT. This paper analyses how control strategies for fatigue life extension can compensate for differing fatigue loads due to varying site conditions. Control strategies applicable for both power production and idling situations are analysed, and methodology to reduce undesirable side-effects is proposed. The design case is a 10MW monopile OWT located in 30 meter water depth at the Dogger Bank in the North Sea, and results are based on time-domain simulations performed using an aero-hydro-servo-elastic simulation tool. The results show that, when all the investigated control strategies are utilized, a fatigue damage reduction over the 20-year lifetime of approximately 50% is possible. Furthermore, it is shown that adverse side-effects such as wear of pitch actuators and fluctuations in the power output can be significantly reduced by limiting the use of control strategies to some predefined situations. With only moderate cost to other system components, the control system is able to compensate for 20% variation in soil stiffness, and 5% (1.5 meter) variation in water depth.

*Keywords:* Offshore wind energy, Foundation design, Controller design, Site-specific conditions, Fatigue load reduction

**Abbreviations**

| | |
|---|---|
| AAD | Active aerodynamic damping |
| AGT | Active generator torque control |
| AIC | Active idling control |
| DEL | Damage equivalent load |
| DLC | Design load case |
| ELC | Environmental load case |
| FLS | Fatigue limit state |
| OWT | Offshore wind turbine |
| RNA | Rotor-nacelle assembly |
| SCO | Soft cut-out |
| TMD | Tuned mass damper |
| ULS | Ultimate limit state |

## 1. Introduction

The offshore wind industry is continuously progressing towards larger wind turbines, with the first 8MW wind turbines grid-connected in 2016 [1]. Larger wind turbines require larger support structures, which without considering the cost of installation, is a component that represents close to 20% of the total cost of offshore wind farms [2, 3]. Monopiles remain the favoured choice of foundation with a market share of 88% in Europe [1], and this trend is expected to persist for wind turbines installed in shallow and intermediate water depths (< 40 meters) [4]. Monopile dimensions are mainly driven by fatigue considerations, and the increase in fatigue loads resuting from the upscaling

*Corresponding author
*Email address:* emil.smilden@ntnu.no (Emil Smilden)

of turbines in combination with deeper water, is a challenge for the economical feasibility of monopile foundations [5]. In particular, large monopiles are more susceptible to fatigue damage from first order wave loads. The magnitude of the hydrodynamic loads increases due to the larger diameter of the monopile. Furthermore, the increased mass of the rotor-nacelle assembly (RNA) and height of the wind turbine, together with a reduction of the rotor speed and the corresponding frequency constraint imposed by the blade passing frequency (3P), pushes the first modal frequencies of the support structure closer to typical wave frequencies [6, 7].

The wind turbine's blade pitch and generator torque control system influences the dynamic response of the structure. The design process for offshore wind turbines (OWTs) should therefore be carried out in an integrated manner, including the design of control strategies that aim to reduce fatigue loads in the support structure [5]. Monopile OWTs are lightly damped, with typical damping ratios in the range 1%-2.5% of critical for the first fore-aft and side-side vibration modes [8, 9, 10]. Aerodynamic damping from the rotor is an important contribution to the overall damping of the fore-aft vibration modes, and several control strategies that are based on enhancing the aerodynamic damping to reduce fatigue loads have been studied [7, 11, 12, 13, 14, 15]. Because the rotor mainly contributes with damping in the fore-aft direction, the support structure is particularly prone to excitation by waves coming from a different direction than the wind. The incidence of environmental conditions with wind/wave misalignment is site-specific, but it can be significant for exposed wind farm locations [16, 17]. Several control strategies that aim to increase the damping of the side-side vibration modes of the support structure have been proposed [7, 11, 13, 18, 19, 14]. The various control strategies for fatigue load reduction are presented in more detail in Section 2.

As demonstrated in [5, 7], control strategies for fatigue load reduction can be integrated in the design process for the support structure, leading to a 9.2% reduction in the weight. A control system that can extend the fatigue life of the OWT can also be used to compensate for uncertainties or simplifications in the design process. The fatigue loading of monopile OWTs is sensitive to variations in site specific conditions such as the water depth and soil properties [20, 21, 22]. Because the water depth and soil properties may vary significantly within a wind farm, it is common industry practice to group the OWTs into clusters, and design the support structures according to the most loaded location in the cluster [23]. The conservatism of this approach may be reduced by introducing control strategies that can compensate for differing fatigue loads due to varying site conditions. Moreover, such control strategies may be applied to increase the size of the design clusters, thereby reducing the number of customized foundation designs. Because the soil properties are associated with large uncertainties [24, 25], the true modal properties of the support structure, particularly the natural frequencies and damping ratios, are often not known before the wind turbine is installed [9]. Furthermore, long-term cyclic loading may cause accumulated pile displacements and changes in the soil properties, thereby changing the modal properties over the lifetime of the OWT [22]. Control strategies that extend the fatigue life of the OWT, may reduce the design conservatism resulting from uncertainty in the modal parameters. Moreover, one could equalize the fatigue utilization for the foundations across the wind farm such that the turbines can be decommissioned at the same time without wasting structural reserves.

Control strategies which mitigate fatigue loads in the support structure, can lead to undesirable side-effects in other wind turbine components. The reliability of the pitch system is a concern with control strategies that require additional pitch activity. A survey consisting of 1400 turbine years of operational data for onshore variable speed turbines found the pitch system to be the sub-assembly with the highest failure rate [26, 27]. Moreover, because the pitch system reliability is difficult to predict, it is desirable to limit the use of pitch actuators. Other critical components that may be negatively affected by the control system are the blades, main shaft, gearbox, and generator. These components have lower failure rates, but they cause higher downtimes when they fail [26]. Furthermore, it is essential to maintain power production, with power quality that complies with grid requirements [28]. A compromise between fatigue load reduction and collateral effects can be achieved by limiting the use of control strategies to certain predefined situations. Enabling control strategies in situations where the tower-top vibration frequency is within a frequency band containing the first modal frequency of the support structure was proposed by [29, 30]. Further, [3, 31] proposed enabling control strategies based on information about environmental conditions, and a multi-objective optimization method was developed to establish the trigger criteria.

The main contribution of the present work is the analysis of the applicability of control strategies for fatigue load reduction to compensate for differing fatigue loads due to varying site conditions. As such, only the fatigue limit state (FLS) is considered, not the ultimate limit state (ULS) and serviceability limit state (SLS). This paper also demonstrates the long-term effects of control strategies for fatigue load reduction. A similar study was performed by [7] for a 5MW OWT. In this paper, a 10MW OWT is considered, and by comparing the results, the present work serves as a

verification and extension of previous research. Furthermore, this paper analyses the trade-offs between fatigue load reduction and undesirable side-effects, and proposes a methodology to improve the overall trade-offs associated with the control strategies. The simulation model is based on the 10MW reference wind turbine of DTU Wind Energy [32], and long-term variations in environmental conditions are based on 60 years of hindcast data for a wind farm site at the Dogger Bank in the North Sea [33]. Simulations are performed using the software tool SIMA by SINTEF Ocean with postprocessing in MATLAB by aid of the WAFO toolbox [34].

The paper is organized as follows: In Sec. 2, an overview of control strategies for fatigue load reduction is given, and the studied control strategies are presented in detail. In Sec.3, the simulation setup is described, and controller performance parameters are established. In Sec. 4, the simulation results are presented and discussed. First, the baseline design case is evaluated, and the long-term effects of control strategies are assessed. Next, the trade-offs between fatigue load reduction and undesirable side-effects are investigated, and methodology to improve the overall perfomance is developed. Finally, applicability of control system design to compensate for differing fatigue loads due to varying site condtions, is assessed. The paper is concluded in Sec. 5.

## 2. Control Concepts for Fatigue Load Reduction

### *2.1. Overview of control strategies*

Wind turbines harvest energy between a cut-in wind speed (typical $V_{\mathrm{In}} = 4$ [m/s]) and a cut-out wind speed ($V_{\mathrm{Out}} = 25$ [m/s]) [35]. Depending on the wind speed, the wind turbine control system operates in one of two modes. For wind speeds below the rated wind speed $V_{\mathrm{Rated}}$, the wind turbine is operated with variable rotational speed aiming to track the optimal tip-speed ratio for maximum power output. For wind speeds above the rated wind speed, variable blade pitch angle is applied to control the aerodynamic torque and limit the power output to the power rating of the generator [28].

Various control concepts for reduction of fatigue loads in the support structure were investigated and compared in [7]. Furthermore, a survey was performed by [14] to map existing control methods for mitigation of support structure loads. An overview of some of the control concepts, classified according to operational range and primary direction of the load mitigation action, is given in Fig. 1.

Control strategies for reduction of fatigue loads in the fore-aft direction are all based on enhancement of the aerodynamic damping. For a wind turbine in normal operation, the prevailing strategy is collective pitch control based on tower velocity feedback, referred to here as active aerodynamic damping (AAD) [7, 11, 12, 13, 14, 15]. AAD is effective for reducing fatigue loads in the support structure, but it is associated with some undesirable side-effects, particularly for the pitch actuators. Less prominent side-effects include increased fatigue loads in the hub, blades and drive-train, increased power fluctuations, and a small reduction in energy yield [7]. A control strategy applicable for wind speeds above $V_{\mathrm{Out}}$ is soft cut-out (SCO) [7, 35]. In SCO the wind turbine operates at reduced speed in wind speeds above the nominal cut-out wind speed. A positive secondary effect of SCO is increased energy yield. However, the extended operational range also increase the fatigue loads in the hub, blades and drive-train. SCO may also be combined with control strategies such as AAD to achieve additional reduction of fatigue loads [7, 35].

To reduce fatigue loads in the side-side direction, additional damping in the sideways direction is needed. The two prevailing control strategies are individual pitch control (IPC) [18, 7, 14], and active generator torque control (AGT) [7, 11, 13, 18, 19, 14]. With IPC, the damping is increased by aid of the rotor, and with AGT the damping is increased by a roll moment from the generator counteracting the sideways vibrations. Both IPC and AGT perform well with respect to fatigue load reduction, but IPC has more severe side-effects than AGT. IPC cause increased wear of pitch actuators, some reduction in energy yield, and increased fatigue loads in the fore-aft direction [18]. Moreover, an additional extreme load check for transient situations such as shut-downs is necessary due to the asymmetric operation of the rotor [7]. Collateral effects of AGT are increased fatigue loads in the drive-train components such as the main shaft and gearbox, and increased power fluctuations [18].

When the wind turbine is parked, either due to a fault, or when the wind speed is outside the operational range, control concepts that require active use of control system actuators can normally not be used. Load mitigation concepts available for wind turbines in idling state (parked) are active idling control (AIC), passive structural dampers, and semi-active structural dampers [7, 14]. When the wind turbine is idling, the rotor is approximately at stand-still with the blades pitched to feather (90°). With AIC, the aerodynamic damping contribution from the rotor is increased by

maintaining a pitch angle < 90° and allowing the rotor to rotate at low speed [7, 14]. Important side-effects of AIC are increased fatigue loads in the blades [7]. Passive and semi-active structural dampers such as mass dampers, oil dampers, or magnetorheological dampers, have the advantage that they do not significantly affect other wind turbine components. They do, however, introduce additional investment costs due to additional structural design requirements, installation, maintenance, and the cost of the damper itself [7].

The control strategies investigated further are AAD for reduction of fatigue loads in the fore-aft direction, AGT for reduction of fatigue loads in the side-side direction, SCO for reduction of fatigue damage in environmental conditions above the nominal cut-out wind speed, and AIC to reduce the impact of idling situations on the fatigue life of the OWT. The baseline OWT is also assumed to be equipped with a tuned mass damper (TMD) that provides the support structure with addtional structural damping. The baseline wind turbine controller is based on the DTU Wind Energy controller presented in [36].

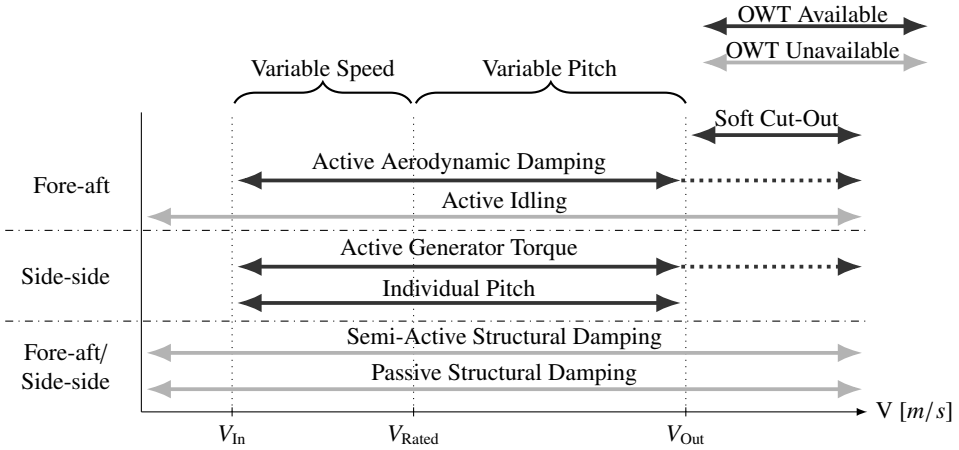


Figure 1: Operational ranges of control concepts for load mitigation [7]. Black arrows indicate control concepts that require the OWT to be operational, and light grey arrows indicate control concepts that are effective also when the OWT is in idling state.

### *2.2. Active aerodynamic damping control (ADD)*

The OWT coordinates and the external loads acting on the support structure are presented in Fig. 2. The hydrodynamic excitation forces are gathered in $F_H(z)$, and decomposed according to the wind/wave misalignment angle $\psi$. The hydrodynamic loads act on the foundation from the seabed ($z = -d$) to the instantaneous free surface ($z = \zeta$). The aerodynamic thrust $F_A(\tilde{v}, \beta, \omega_R)$ is applied at the tower top $z = h$, and is a function of the relative wind speed $\tilde{v}$, blade pitch angle $\beta$, and rotor speed $\omega_R$.

Pitch control action modifies the effective damping of the fore-aft vibration modes of the support structure through the aerodynamic thrust. If information about the tower top velocity is available it is possible to design a pitch controller that enhances the aerodynamic damping by increasing the thrust force when the tower top has an upwind velocity, and vice versa. If only acceleration measurements are available, an estimate of the velocity needs to be obtained by integration of the acceleration signal [12]. The AAD controller and the nominal controller are treated as two independent controllers, and their demanded pitch actions are superimposed. To deal with possible coupling between the two controllers, the nominal controller needs to be retuned with the AAD controller activated [13].

Following the approach of [11, 12], the control law for the AAD pitch actions is derived based on the second order differential equation describing the response of the support structure in its first fore-aft vibration mode. The resulting control law is given by

$$\beta_{AAD} = -\frac{1}{F_A^{\beta}(\omega_R, \beta)} \frac{\eta(\omega_R, \beta) K_{AAD}}{q(h)} \dot{x} \tag{1}$$

where $K_{AAD} \geq 0$ is the controller gain, $\dot{x}$ is the measured tower top fore-aft velocity, and $q_x(h) > 0$ is the first fore-aft mode shape of the support structure at height $h$. The AAD control actions are scaled by the partial derivative from

pitch to aerodynamic thrust $F_A^\beta(\omega_R,\beta) < 0$. In addition, the gain scheduling factor $\eta(\omega_R,\beta) \geq 0$ is included to allow for the AAD controller to be tuned separately for a range of wind speeds. In reality, both $F_A^\beta(\omega_R,\beta)$ and $\eta(\omega_R,\beta)$ depend on the free stream wind velocity $v$. In order to avoid the use of uncertain wind speed measurements, this dependence is removed by expressing $v$ as a function of the controlled parameters $\beta$ and $\omega_R$.

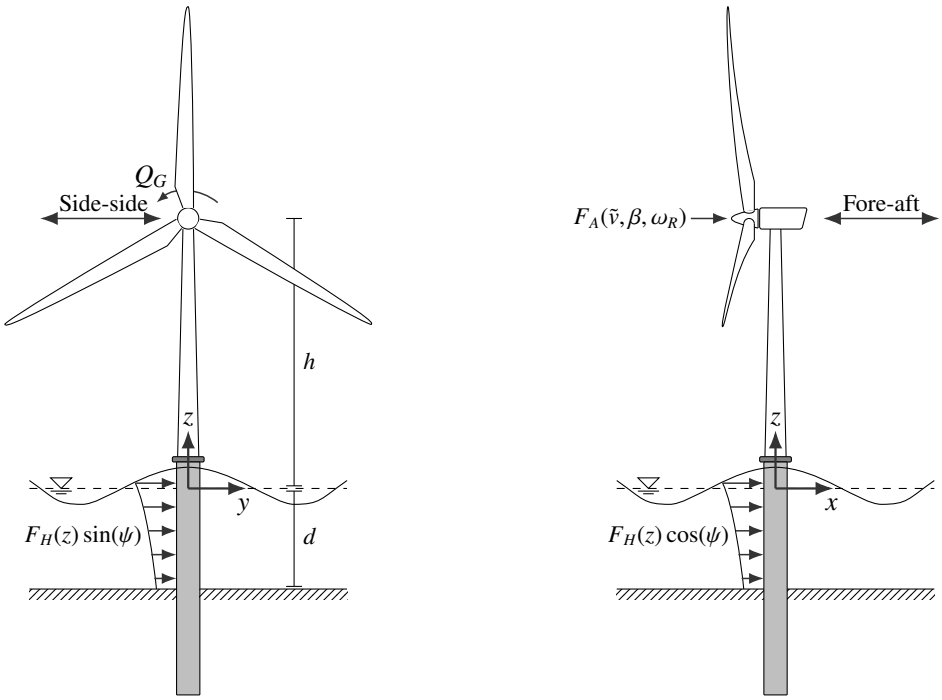


(a) Front view. (b) Side view.

Figure 2: Definition of wind turbine coordinates and excitation forces.

### *2.3. Active generator torque control (AGT)*

The generator torque affects the side-side motion of the support structure through the reaction on the generator stator, which is fixed to the main frame at the tower top. It is therefore possible to increase the damping of the side-side vibration modes of the support structure by controlling the generator torque in opposite phase with the side-side velocity [19]. Similar to the AAD controller, the nominal controller and the AGT controller are treated as two independent controllers, and their demanded generator torque actions are superimposed [13]. The speed variation caused by the AGT controller may cause undesirable coupling with the nominal pitch controller, which is mitigated by limiting the gains of the AGT controller [7, 18].

The control law for the AGT control actions is derived based on the second order differential equation describing the response of the support structure in its first side-side mode. Neglecting the friction in bearings and the gearbox [19], the only loads acting in the side-to-side direction are wave loads, and the generator torque $Q_G$. By introducing a feedback from the side-side tower top velocity $\dot{y}$ to the generator torque, the following control law is proposed:

$$Q_{AGT} = -\frac{K_{AGT}}{q_y'(h)}\dot{y} \tag{2}$$

where $K_{AGT} \geq 0$ is the controller gain, and $q_y(z)$ is the first side-side vibration mode of the support structure at vertical position $z$. The constant $q_y'(h) > 0$ is the partial derivative of $q_y(z)$ with respect to $z$ at height $h$.

### 2.4. Soft cut-out (SCO)

When the cut-out wind speed is exceeded for a specified period of time, a shut down procedure is triggered, and the wind turbine is switched to idling mode and disconnected from the grid [14]. For an onshore wind turbine, the cut-out wind speed is defined based on a compromise between the lifetime power production, and the addtional cost introduced by designing the wind turbine to withstand the loads imposed by operation in high wind speeds [35]. However, for offshore wind turbines, the loads, particularly in the support structure, are not necessarily reduced by shutting down the wind turbine. For support structure designs suffering from wave induced fatigue loads, the lack of aerodynamic damping in severe environmental conditions may be responsible for a considerable contribution to the lifetime accumulated fatigue damage [7].

Though there are multiple advantageous consequences of SCO, the main focus of this paper is the effect of SCO in terms of fatigue damage in the support structure. Multiple strategies for SCO exist [5, 7, 14, 35]. Typically, a downrating of the wind turbine is performed by a gradual reduction of the rotor speed, either stepwise [5, 7], or continously [35]. The aim is to limit the aerodynamic loads to avoid an increase in possible design-driving ultimate loads, and to reduce the risk of rotor over-speed events [5]. Similar to [5, 7], a single stepwise reduction of the rotor speed to 80% of the nominal rated value is performed. This corresponds to a downrating of the wind turbine to 8MW. The generator torque input is proportional to the power reference. In order to reduce the magnitude of generator torque fluctuations by approximately $\approx 10\%$, the power reference is further reduced to 7MW.

### 2.5. Active idling control (AIC)

Normally, the blades are pitched to feather (90°) during idling in order to minimize the aerodynamic loading of the rotor. Consequently, negligible fore-aft aerodynamic damping is present when the wind turbine is parked. By maintaining a pitch angle $< 90°$, the aerodynamic loads on the rotor are increased, resulting in a considerable damping contribution to the fore-aft vibration mode [7]. In the present work, AIC is performed with the blades pitched to some prescribed setting. The pitch actuators are therefore not required to be functional. However, some types of actuator faults may still prevent AIC. If, for example, one or more of the pitch actuators are stuck, the asymmetric loading of the rotor may cause unacceptably large vibration in the RNA and the support structure. AIC does not require the generator to be grid-connected, but the shaft must be free to rotate without faults in the drive-train including the gearbox. Furthermore, the rotor must be aligned with the wind direction, which requires the yaw system to be functional. In [27], these components were found to contribute to the total downtime by 10% for the yaw system, 5% for the drive-train module including the gearbox assembly, and 20% for the pitch system. Assuming that only half the pitch system faults prevent the use of AIC, the rotor is allowed to rotate during 75% of the time the OWT is parked with fault. The remaining 25% is normal idling with the blades pitched to feather.

Selecting the pitch angle for AIC involves a trade-off between the rotor speed and the magnitude of the damping contribution. Higher allowable rotor speeds increase the damping contribution, and vice versa. In the present work, a constant pitch angle of 40° is applied. With a constant pitch angle of 40°, the rotor speed is approximately 0.9 [rad/s] at $V = 40$ [m/s], which is below the rated rotor speed $\omega_{\text{Rated}} = 1.005$ [rad/s]. It is assumed that this is a reasonable upper limit for the wind speeds encountered during AIC. An issue emerging from AIC is the interaction between the 3P frequency and the first fundamental frequency of the support structure. In the present work, this problem is not addressed specifically, however, initial investigations show that the fatigue loads resulting from this issue are small.

### 2.6. Support structure damping and tuned-mass damper (TMD)

Neglecting aerodynamic damping from the rotor, the predominant global damping contributions for monopile OWTs are material damping, soil damping, hydrodynamic damping, aerodynamic tower damping, and additional damping devices such as a tower oscillation damper [8]. Several studies have been performed to estimate the damping ratios for monopile OWTs, and particularly the damping contribution emerging from soil-structure interaction. The total system damping was estimated from rotor stop tests in [8]. The study considered data from more than 1500 tests divided between four different wind parks with soil conditions similar to the Dogger Bank. The results showed an average total damping ratio of $\approx 2.5\%$, where $\approx 1\%$ was attributed to soil damping, and $\approx 0.4\%$ was attributed to material-, hydrodynamic- and aerodynamic tower damping. All wind turbines were equipped with a structural damping device which was assumed to contribute with the remaining $\approx 1.1\%$. Similar, but slightly lower damping ratios were observed by [9, 10], which investigated rotor stop tests performed on an offshore wind turbine placed in

a location with soil mainly consisting of sand. The structural damper was turned off during the tests, and the total damping ratio was estimated as $\approx 1.0\%$. Furthermore, [37] concluded that soil-structure interaction contributed with damping in the range 0.17%-0.72% for soil conditions that are typical for the North Sea. Based on these results, the damping ratio for the support structure is taken as 1.1%, where 0.5% is due to material-, hydrodynamic- and aerodynamic damping, and 0.6% is due to soil damping. Two TMDs are included in the simulation model, increasing the damping ratio for the first fore-aft and side-side vibration modes to 2.2%. The TMDs are located in the top of the tower, and the TMD mass is 20 tonnes, corresponding to approximately 2% of the modal mass for the first fundamental mode. The natural frequency of the dampers are tuned to the natural frequency of the first fundamental mode, and a configuration with two independent dampers in the fore-aft and side-side direction is used, following [38].

## 3. Simulation Setup

This section is organized as follows: First, a procedure for establishing an environmental design basis is presented. Next, the design load cases are selected according to the standard [39]. Further, the simulation model is presented, and the procedure for estimation of support structure fatigue damage is explained. Finally, the comparison parameters that will be used to assess the performance of control strategies are established.

### *3.1. Environmental conditions*

A wind farm site at the Dogger Bank in the North Sea is chosen as the design location. Hindcast data for a period of 60 years with a resolution of 3 hours, are provided by the Norwegian Meterological Institute. Details regarding the hindcast, which covers the North Sea, the Norwegian Sea, and the Barents Sea, are found in [33]. Furthermore, a detailed statistical description of the metocean data for the design location is given in [17], and some important features with regard to assessment of the lifetime fatigue strength are presented in [6]. The metocean data contains information about significant wave height $H_s$, peak period $T_p$, wave direction, mean wind speed $V$, and wind direction. Turbulence intensity and wind shear, which were not considered in the hindcast, are accounted for in accordance with [40]. A complete assessment of the lifetime fatigue strength of the support structure should include long-term variations in at least: $H_s$, $T_p$, $V$, wind direction, wave direction, and turbulence intensity. The number of environmental parameters can be reduced to four by assuming the turbulence intensity to be a function of $V$, and introducing the misalignment angle $\psi$ as the relative angle between the wind and wave direction. Even with the reduction of environmental parameters, it is computationally impracticable to consider all possible combinations. A procedure for lumping of environmental conditions to environmental load cases (ELCs) is therefore developed:

**Step 1. Grouping of metocean data:** To reduce the number of environmental conditions, the metocean data is distributed into a three dimensional collection of bins, based on the environmental parameters $V$, $\psi$, and $H_s$. Starting with wind speed $V$, a bin size of 2 [m/s], in accordance with [39], is used. Further, the wind/wave misalignment $\psi$ is divided into sectors of 30° as shown in Fig. 3, with wind always coming from 0°, and waves coming from $0°, 30°, \ldots, 180°$ [6]. Following [3], the number of bins are halved by merging the sectors mirrored about the vertical axis. For each of the $16 \times 7 = 112$ combinations of $V$ and $\psi$, three sea states are considered. The resulting number of ELCs are $16 \times 7 \times 3 = 336$. However, after removing the environmental conditions with occurrence probability less than $1 \times 10^{-4}$, the number is reduced to 138.

**Step 2. Wind conditions:** A reliable estimate of the lifetime accumulated fatigue damage cannot be achieved by coarsely grouping the metocean data and only considering the center value of each bin. For each bin, an equivalent load case that represent the fatigue damage from all the observed combinations of environmental conditions within the bin. When the wind turbine is not operating, the aerodynamic contribution to fatigue damage is negligible, and the center value can be taken as a representative wind speed. In operation, the aerodynamic response of the wind turbine may be assumed independent of the sea state. It is therefore acceptable to estimate the aerodynamic contribution to fatigue damage for different wind speeds without considering hydrodynamic loads [41]. Short-term fatigue damage is computed for wind speeds between $V = 4$ [m/s] and $V = 26$ [m/s] with 1 [m/s] intervals based on 1-hour simulations. Further, the results are weighted by the long-term distribution of wind speed. The equivalent wind conditions are found as the center of mass for each wind speed bin calculated from the long-term distribution of fatigue damage.

**Step 3. Wave conditions:** Due to the wind speed dependent aerodynamic damping, the hydrodynamic contribution to fatigue damage depends on the wind conditions. When the wind turbine is operating, the aerodynamic damping of the fore-aft vibration modes reduces fatigue loads compared to a wave-only condition [41]. Here, the hydrodynamic contribution to fatigue damage is considered without taking into account the effect of aerodynamic damping. The result is a moderate shift in $H_s$ and $T_p$ towards higher sea states with wave frequencies closer to the first modal frequency of the support structure and a conservative set of ELCs. An alternative method based on hydrodynamic transfer function combined with an iterative procedure is described in [41]. This method would produce less conservative load cases, but requires a set of hydrodynamic transfer functions to be derived for each wind speed bin. The method is further complicated by the load mitigation controllers because they change the response of the wind turbine to hydrodynamic loads. Similar to the wind conditions, the short-term fatigue damage is computed for different combinations of $H_s$ and $T_p$ with 0.5 [m] intervals for $H_s$, and 1 [s] intervals for $T_p$. The weighted fatigue damage is then found for each combinations of $V$ and $\psi$, and the equivalent wave conditions are found as the center of mass for each sea state class calculated from the long-term distribution of fatigue damage.

The procedure for lumping of ELCs is summarized in Fig. 4, and the resulting ELCs are given in Appendix B.

The wave time series are generated based on the JONSWAP spectrum with the peak enhancement factor $\gamma$ given by $H_s$ and $T_p$ in accordance with [42], and long-crested waves are assumed. The three-dimensional turbulent wind fields are generated based on the Kaimal spectrum using the full-field turbulence simulator TurbSim by NREL [43]. The Class B normal turbulence model (NTM) is assumed, and the wind shear is modeled by a power law with shear exponent 0.14 [40].

Simulations are performed with a duration of 3900 seconds, with the first 300 seconds removed to exclude the start-up transients. For each ELC, two random seeds are used, resulting in a total simulation time of two hours.

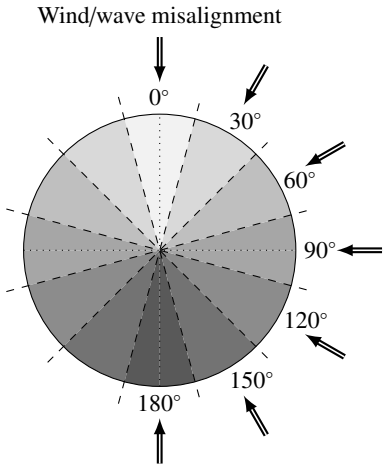


Figure 3: Wind/wave misalignment bins, with wind from 0° and waves from 0°, 30°, . . . , 180°. Bins with the same shade of grey are merged [3, 6].

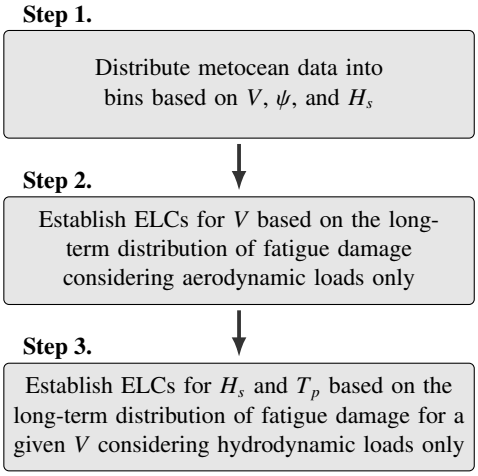


Figure 4: Procedure for establishing lumped environmental load cases (ELCs).

### *3.2. Design load cases*

The design load cases (DLCs) considered for calculation of the lifetime accumulated fatigue damage are given in Table 1. Situations such as startup and shutdown, or occurrence of failure modes, are assumed to have small contributions to fatigue damage over the lifetime of the support structure, and design load cases concerning these situations are disregarded [7]. Furthermore, design load cases concerning operation with ice formation, and transport, installation, maintenance, and repair, are also disregarded.

In DLC 7.2 the wind turbine is idling after the occurrence of a fault. It is assumed that the availability of the wind turbine is independent of environmental conditions, and that the total availability is 90%, following the recommendation of [39]. DLC 7.2 therefore accounts for 10% of the lifetime, evenly spread over all environmental conditions. An

availability ratio of 90% is a conservative estimate, and contractual availability of 95% is common for offshore wind turbines [44].

When the wind turbine is operating (DLC 1.2), or is parked without fault (DLC 6.4), the yaw system is active. Following the recommendation of [39], yaw errors of ±8° are introduced in the simulations to account for the hysteretic behaviour of the yaw system. When the wind turbine is parked with fault (DLC 7.2) the yaw system cannot be assumed active. Due to limitations of the simulation tool and implemented theory, large yaw misalignments give unreliable results. Yaw errors of ±8° are therefore assumed also for DLC 7.2.

Table 1: Design load cases (DLCs) for FLS analysis recommended by the standard by DNV GL [39]. NTM refers to normal turbulence model, NSS refers to normal sea state, MUL refers to multidirectionality of environmental condtions, and MIS refers to wind/wave misalignment.

| DLC | Design situation | Wind condition | Wave condition | Directionality | Description |
|---|---|---|---|---|---|
| 1.2 | Power production | NTM $V_{in} < V < V_{out}$ | NSS | MUL MIS | Normal operation, with no faults, and with a functional control system |
| 6.4 | Parked | NTM $V < V_{in}$ $V > V_{out}$ | NSS | MUL MIS | Idling below cut-in wind speed or above cut-out wind speed |
| 7.2 | Parked with fault | NTM $V_{in} < V < V_{out}$ | NSS | MUL MIS | Idling after the occurrence of a fault |

### *3.3. Simulation model*

The wind turbine is modeled in the aero-hydro-servo-elastic simulation tool SIMA by SINTEF Ocean. The structural model comprising the foundation, tower, and blades, is modeled using nonlinear beam elements that accounts for large deformations [4]. The soil stiffness is modeled using nonlinear springs with stiffness properties computed from pressure-displacement curves. The soil profile is based on conditions at the Dogger Bank with a 1.5 meter top layer of cohesionless soil (sand) followed by cohesive soils (clay). The pressure-displacement curves are computed according to [45] using the most conservative (lowest) estimate of the clay shear strength. The material-, hydrodynamic- and aerodynamic damping is accounted for by stiffness-proportional Rayleigh damping distributed along the complete support structure, and the soil damping is accounted for by increasing the Rayleigh damping in the foundation beneath the mudline.

Aerodynamic loads are modeled using blade element momentum (BEM) theory with corrections for tip loss, hub loss, dynamic inflow, dynamic wake, skewed inflow, and tower shadow [46]. Hydrodynamic loads are calculated based on Morison's equation accounting for relative velocities and assuming Airy linear wave theory with the wave kinematics integrated to the instantaneous free surface [47]. In all simulations, the inertia coefficient is taken as $C_M = 2$ and the quadratic drag coefficient is taken as $C_D = 0.9$ [4]. The simulation model is based on the 10MW reference wind turbine of DTU Wind Energy [32] placed on a monopile foundation with diameter 8.5 meters. The monopile is placed in 30 meter water depth, and the total depth of the monopile is 42 meters below the seabed. The wind turbine tower is stiffened compared to the tower in [32] through a 20 % increase in wall thickness [4]. The first modal frequencies of the support structure are 0.214 Hz for the fore-aft mode, and 0.213 Hz for the side-side mode.

### *3.4. Support structure fatigue calculation*

The lifetime accumulated fatigue damage is computed by combining short-term estimates of fatigue damage with the long-term variations in environmental conditions. The short-term fatigue damage is calculated based on rainflow counting of stress cycle amplitudes [48], and summation of fatigue damage based on the S-N approach following the Palmgren-Miner linear damage hypothesis. The short-term time histories of stress in the support structure are computed from time histories of bending moments and internal forces obtained from SIMA. Only the fatigue contribution

from axial stress is considered. The post processing of stress histories is performed in MATLAB using the WAFO implementation [34] of rainflow counting, the S-N method and Palmgren-Miner summation modified to account for a bi-linear S-N curve.

The S-N curve recommended by [49] for steel in water with cathodic protection is applied. Because fatigue damage is likely to occur in in weld details rather than in the base material, detail category D is used [4]. The applied S-N curve is bi-linear with exponent 5 for high-cycle fatigue and exponent 3 for low-cycle fatigue. Stress calculations are performed with a stress concentration factor of 1. Higher stress concentration factors may be applicable for some sections of the support structure such as the tower top, the intersection between the tower and the transition piece, or at the mudline. This is, however, disregarded for simplicity, since the focus is on comparison of control strategies.

Locations along the support structure that are critical with regard to fatigue strength are the foundation beneath the mudline, and in the intersection between the tower and the transition piece [7, 4, 6]. It is required by [50] to use a safety factor of 3 for non-accessible areas, which applies for the foundation, but not the tower. Based on initial investigations, the foundation is taken as the critical component with regard to fatigue failure. The cross-section 6 meters below the mudline was found to have the highest fatigue utilization.

### *3.5. Performance comparison parameters*

Several representative parameters related to different wind turbine components are used to evaluate the performance of the load mitigation strategies. All performance parameters are presented by comparison with the baseline case, expressed in percentage. The performance comparison parameters and their desired trend are summarized in Table 2. For all components it is desirable to limit the increase in performance parameters as much as possible, except from the power output. Because the actual fatigue utilization of the foundation is estimated, and a bi-linear S-N curve is applied for the fatigue calculations, fatigue damage ($D$) is used as performance measure for the support structure. For the other components, damage equivalent load (DEL) is used. It is stressed that changes in $D$ and DEL are scaled differently. For a given S-N slope exponent $p$, the relationship between a change in fatigue damage $\Delta D$ and fatigue load $\Delta$DEL is given by

$$\Delta\text{DEL} = \Delta D^{\frac{1}{p}} \tag{3}$$

Table 2: Performance comparison parameters and their desired trend, classified according to system components. A downward pointing arrow indicates that the desired trend is a reduction of the performance parameter, and vice versa.

| Component | Performance parameter | Description | Desired trend |
|---|---|---|---|
| Support structure | $D^{20}_{\text{Max}}$ | Maximum fatigue damage | $\downarrow$ |
| | $D^{20}_{\text{FA}}$ | Fore-aft fatigue damage | $\downarrow$ |
| | $D^{20}_{\text{SS}}$ | Side-side fatigue damage | $\downarrow$ |
| Blade root | $\text{DEL}^{20}_{\text{Edge}}$ | Edgewise fatigue loads | $\downarrow$ |
| | $\text{DEL}^{20}_{\text{Flap}}$ | Flapwise fatigue loads | $\downarrow$ |
| Pitch actuators | $\text{DEL}^{20}_{\beta}$ | Actuator bearing fatigue loads | $\downarrow$ |
| | $\text{ADC}^{20}_{\beta}$ | Actuator duty cycle | $\downarrow$ |
| Drive-train | $\text{DEL}^{20}_{\text{Gear}}$ | Gear tooth fatigue loads | $\downarrow$ |
| | $\text{DEL}^{20}_{\text{Shaft}}$ | Shaft fatigue loads | $\downarrow$ |
| Power production | $P^{20}_{\text{Out}}$ | Power output | $\uparrow$ |
| | $P^{20}_{\text{Std}}$ | Standard deviation of power output | $\downarrow$ |

The maximum 20-year accumulated fatigue damage ($D^{20}_{\text{max}}$) in the critical foundation cross-section, is taken as the primary measure of control strategy performance in terms of support structure fatigue damage. In addition, the 20-year accumulated fatigue damage in the fore-aft direction ($D^{20}_{\text{FA}}$) and the side-side direction ($D^{20}_{\text{SS}}$) in the critical cross-section, is computed to investigate how the control strategies affect the fore-aft and side-side vibration modes. Wind speed directionality is disregarded from the analysis in order to compute $D^{20}_{\text{FA}}$ and $D^{20}_{\text{SS}}$ (only the relative wave direction is considered). The full lifetime fatigue damage considers both effects around the full circumference of the

foundation.

Further, the blade root fatigue loads are considered. The flapwise and edgewise lifetime weighted damage equivalent load, denoted as $\mathrm{DEL}^{20}_{\mathrm{Edge}}$ and $\mathrm{DEL}^{20}_{\mathrm{Flap}}$, are computed from the time histories of blade root bending moments. The long-term DEL for a load $S$ over $k$ number of ELCs is calculated according to

$$\mathrm{DEL}^{20} \propto \left( \sum_{i}^{k} P[i] \sum_{j}^{n_i} S_j^p n_j \right)^{\frac{1}{p}} \tag{4}$$

where $p$ is the slope of the S-N curve, $n_j$ is the number of load cycles at load range $S_j$ [48], and $n_i$ is the number of load ranges for ELC $i$ with probability $P[i]$. Because only the relative value compared with the baseline case is used, all constants are ommited from the expression in Eq. (4). The number of load cycles per load range is determined by use of rainflow counting, with an S-N slope of $p = 10$ following [51].

The main concern related to pitch activity is wear of the pitch actuators. According to [15, 52], a rough estimate of the fatigue damage in the pitch bearings, which are typically critical components of the pitch actuator, is given by the DEL over $N$ revolutions of the bearing, given by

$$\mathrm{DEL}_{\beta} = \left( \frac{1}{N} \sum_{j} |M_{o,j}|^p n_j \right)^{\frac{1}{p}} \tag{5}$$

where $M_o$ is the overturning moment in the pitch bearing, $n_j$ is the number of revolutions of the pitch bearing at loading level $M_{o,j}$, and the exponent $p$ is a bearing type-specific parameter. The stress range and counting of stress cycle amplitudes for bearing and gearing is fundamentally different to that of other wind turbine components. Whereas fatigue damage in the support structure or the blades is governed by fluctuations in the external loads, the fatigue damage in bearings or gears is governed by input load level and the rate and number of revolutions of the component [53, 54]. Following a similar approach as in [15], the sum is taken over each time step with the increment in pitch angle taken as $n_j$. The long-term wear of the pitch actuator bearings for $k$ number of ELCs is then given by

$$\mathrm{DEL}^{20}_{\beta} \propto \left( \sum_{i}^{k} P[i] \int_0^T |M_{o,i}(t)|^p |\dot{\beta}_i(t)| \, dt \right)^{\frac{1}{p}} \tag{6}$$

where $M_{o,i}(t)$ and $\dot{\beta}_i(t)$ are the time histories of overturning moment and blade pitch rate for ELC $i$ with probability $P[i]$ and duration $T$. The exponent $p = 3$ is used corresponding to typical S-N curves for ball bearings [52]. Furthermore, it is desirable to include also a measure of the lifetime use of the pitch actuators. A measure used to quantify pitch actuator use over a time period of duration $T$, is the pitch actuator duty cycle $\mathrm{ADC}_{\beta}$, defined in [55] as

$$\mathrm{ADC}_{\beta} = \frac{1}{T} \int_0^T \frac{|\dot{\beta}_i(t)|}{\dot{\beta}_{max}} \, dt \tag{7}$$

where $\dot{\beta}_{max} > 0$ is the maximum allowable pitch rate. Computing $\mathrm{ADC}_{\beta}$ for each ELC, and summing over the lifetime, yields the following expression for the lifetime use of the pitch actuators:

$$\mathrm{ADC}^{20}_{\beta} \propto \sum_{i}^{k} P[i] \int_0^T |\dot{\beta}_i(t)| \, dt \tag{8}$$

It can be seen from the expression in Eq. (8) that $\mathrm{ADC}_{\beta}$ is a measure of the distance traveled for the pitch actuator.

The fatigue life of drive-train components is affected by both additional generator torque variations and aerodynamic torque variations caused by additional pitch activity. The drive-train is represented by a lumped mass model accounting for generator inertia, and shaft torsional flexibility. Although the simulation model does not include a detailed description of the gearbox, rough estimates of the fatigue loads in both the shaft and the gearbox may be computed based on the global torsional loads obtained from the lumped mass model. First, the gear tooth root bending fatigue is considered. Following the method described in [53], the internal gear dynamic effects are neglected, and the gearbox transmitted force is given by

$$F_{GB} = \frac{2}{d_1} \Big( Q_A - (I_R + N_G^2 I_G) \dot{\omega}_R \Big) \tag{9}$$

where $d_1$ is the gear pitch circle diameter, $I_R$ and $I_G$ are the rotor and generator torsional moments of inertia, $N_G$ is the gear ratio, $\dot{\omega}_R$ is the rotor angular acceleration, and $Q_A$ is the aerodynamic torque on the main shaft. A single gear tooth goes into contact once every revolution of the gear, causing the tooth root bending stress or surface pitting stress to fluctuate between zero and a peak value corresponding to the gear input load [53]. Following the recommendation of [56], the load spectra for the gearbox should be determined by use of the load duration distribution method (LDD). According to [57, 53] the gear tooth root bending stress can be assumed to vary between zero and a peak value proportional to the gear transmitted force given by Eq. (9). The time series obtained from short-term simulations are therefore divided into bins depending on the load level, and the fatigue damage is determined by the number of gear revolutions at each load level. Similar to the pitch bearing, the DEL at $N$ revolutions of the gear can be formulated as

$$\mathrm{DEL}_{\mathrm{Gear}} = \left( \frac{1}{N} \sum_j |F_j|^p t_j \omega_j \right)^{\frac{1}{p}} \tag{10}$$

where $F_j$ is the load level given by the upper value of bin $j$, $t_j$ is the time duration of the bin, and $\omega_j$ is the average gear angular speed within the bin. The expression in Eq. (10) can be expressed on continous form by assuming infinite load levels and taking the sum over each time step. The lifetime DEL of the gear is then given by

$$\mathrm{DEL}^{20}_{\mathrm{Gear}} \propto \left( \sum_i^k P[i] \int_0^T F_{GB,i}(t)^p \omega_i(t)\, dt \right)^{\frac{1}{p}} \tag{11}$$

where $F_{GB,i}(t)$ and $\omega_i(t)$ are time histories of gear transmitted force and gear angular speed, and S-N slope exponent $p = 6.225$ is applied following [53]. The torsional fatigue loads in the drive-train shaft, denoted as $\mathrm{DEL}^{20}_{\mathrm{Shaft}}$, are also computed from the gear transmitted force in Eq. (9). Similar to the blade roots, the long-term DEL for the shaft is calculated according to Eq. (4) with rainflow counting of stress amplitudes. The S-N slope exponent $p = 3$ is used as suggested by [58].

In addition to fatigue loads in wind turbine components, the lifetime energy yield $P^{20}_{\mathrm{Out}}$, and lifetime weighted standard deviation in the power output $P^{20}_{\mathrm{Std}}$ are included as performance measures to investigate how the power output is affected by the control strategies that are active during power production.

## 4. Simulation Results

The simulation results are organized as follows: First, the results of the baseline design case are evaluated to identify the key contributors to fatigue damage in the support structure. The results give an indication of the potential for fatigue load reduction with the various control strategies, and aid to understand the results presented subsequently. Next, the lifetime effects of the different control strategies are analysed, and the performance is evaluated based on the comparison parameters established in Sec. 3.5. Further, the trade-offs between fatigue load reduction and undesirable side-effects are investigated. The aim is to explore the potential of situational use of control strategies to improve the overall performance. Based on the results, some trigger criteria for enabling control strategies are established. In the subsequent analysis, these trigger criteria are employed to achieve a desired level of fatigue load reduction at minimum cost to other system components. Finally, the ability of the control system to compensate for differing fatigue loads due to varying site conditions is analysed.

### *4.1. Baseline Design Case Evaluation*

The radial distribution of lifetime accumulated fatigue damage in the foundation 6 meters below the mudline is presented in Fig. 5. The results are given for different combinations of the DLCs, showing that DLC 1.2 and DLC 7.2 are responsible for the majority of the fatigue damage. Notably, DLC 7.2 contributes with more than 30% of the total fatigue damage, highlighting the importance of wind turbine availability for the fatigue design of monopile foundations. The effect of wind turbine availability depends on the relative importance of aerodynamic and hydrodynamic fatigue loads. A high incidence of rotor idling is positive in terms of aerodynamically induced fatigue loads. The opposite is true for the hydrodynamically induced fatigue loads, which are exacerbated by the lack of aerodynamic

damping when the wind turbine is parked. For the present design case the fatigue damage is dominated by hydrodynamic fatigue loads [6], making DLC 7.2 particularly harmful.

The fatigue damage is nonuniformly distributed around the circumference of the support structure, with southwest/northeast being the most critical orientations. This is expected, as the design location is characterized by a high incidence of wind and wind-sea from southwest [17]. The difference between the minimum and maximum fatigue damage around the circumference of the support structure is, however, only approximately 20%. With a safety factor of 3, the maximum accumulated fatigue damage is 1.2, suggesting that the foundation will fail during 20 years at the design location. There are, however, many uncertainties related to the wind turbine model and the fatigue strength analysis. The fatigue design of the support structure is therefore not further optimized, and it is assumed that the monopile with the chosen dimensions is a realistic representation of a foundation design within the scope of the present work.

The plot in Fig. 5b shows how the fatigue damage is distributed between the fore-aft and side-side vibration modes. The results are given for the total fatigue damage around the full circumference of the foundation, and the participation of the fore-aft and side-side vibration modes at the point of the maximum fatigue damage $D^{20}_{\mathrm{Max}}$, may be different. The fatigue damage in the side-side direction is approximately 20% compared with the fore-aft direction, and there is a negligible contribution to $D^{20}_{\mathrm{SS}}$ from DLC 6.4 and DLC 7.2. The difference between operation and idling in terms of response to hydrodynamic loads is small, and the 80% of the time the wind turbine is in DLC 1.2 is expected to be responsible for the larger share of $D^{20}_{\mathrm{SS}}$. Moreover, due to the larger projected area when the blades are pitched to feather, the aeroelastic damping in the side-side direction is higher when the wind turbine is parked [59, 60]. The absence of fatigue loads due to generator torque variations further reduces the contribution to $D^{20}_{\mathrm{SS}}$ from DLC 6.4 and DLC 7.2.

The contribution to $D^{20}_{\mathrm{FA}}$ and $D^{20}_{\mathrm{SS}}$ as a function of wind/wave-misalignment is given in Fig. 6 together with the lifetime probability of the associated environmental conditons. Environmental conditions with wind/wave-misalignment less than 15° are the main contributors to fatigue damage in the fore-aft direction. Furthermore, DLC 7.2 contributes with approximately 40% of $D^{20}_{\mathrm{FA}}$, meaning that, for a given time duration, DLC 7.2 is on avarage more than 6 times as harmful as DLC 1.2. The fatigue damage in the side-side direction is mainly caused by environmental conditions with wind/wave-misalignment between 15° and 105°. With reference to Fig. B.12, this is due to a combination of moderate probability and severity of the sea states. The contributions to $D^{20}_{\mathrm{FA}}$ and $D^{20}_{\mathrm{SS}}$ are given in Fig. 7 as a function of wind speed. In the fore-aft direction, the majority of the fatigue damage is caused by environmental conditions with wind speeds above the rated wind speed. In the side-side direction, the majority of the fatigue damage is caused by environmental conditions with wind speeds around the rated wind speed. Further, it is observed that the main contribution to $D^{20}_{\mathrm{FA}}$ from DLC 6.4, is from environmental conditions with wind speed above the cut-out wind speed.

The main contributions to fatigue damage in the support structure are summarized in Table 3 together with the primary source of the associated fatigue loads, and the appropriate control strategies for fatigue load reduction. Based on the presented results, AAD and AIC are expected to yield the largest reductions in the lifetime accumulated fatigue damage.

Table 3: Main contributions to fatigue damage in the support structure and associated control strategies for fatigue load reduction.

| DLC | Contribution to $D^{20}_{\mathrm{Max}}$ | Direction of fatigue loads | Source of fatigue loads | Control strategy |
|---|---|---|---|---|
| 1.2 | 61.5% | Fore-aft/side-side | Hydrodynamic/Aerodynamic | AAD/AGT |
| 6.4 | 5.6% | Fore-aft | Hydrodynamic | SCO |
| 7.2 | 32.9% | Fore-aft | Hydrodynamic | AIC |

### *4.2. Long-term evaluation of control strategies*

The control strategies are evaluated by comparison with the baseline case in Table 4. Starting with the effect of AAD, a considerable reduction is achieved for both the fore-aft and the maximum fatigue damage. Noticeably, the

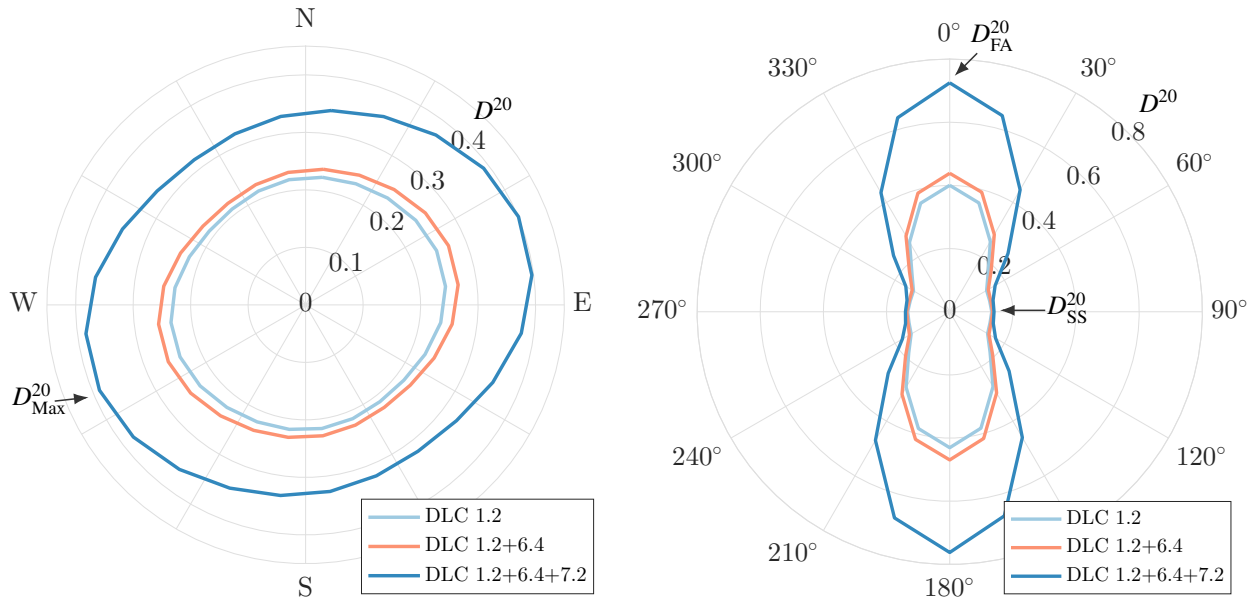


(a) Full lifetime analysis.

(b) Results without wind speed directionality.

Figure 5: Radial distribution of lifetime accumulated fatigue damage in the support structure 6 meters below the mudline for different combinations of design load cases (DLCs). The result of the full lifetime analysis including the directionality of the wind speed is given in the plot to the left, and the results without considering wind speed directionality (wind always from 0°) is given in the plot to the right. The results are presented as combinations of the DLCs with, for example, DLC 1.2+6.4 denoting the results of these two load cases superimposed.

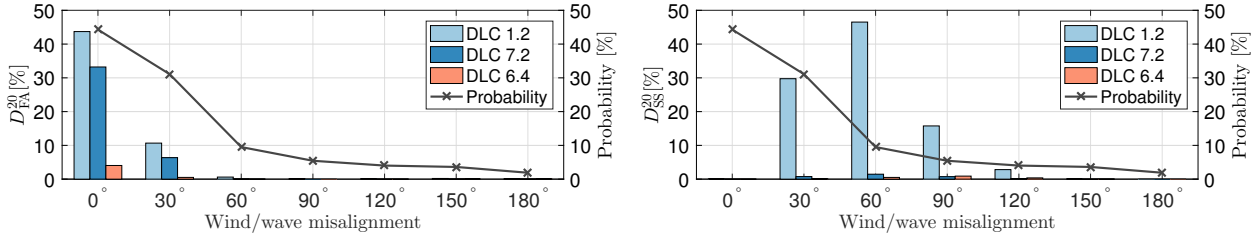


(a) Fore-aft direction.

(b) Side-side direction.

Figure 6: Lifetime probability and contribution to fore-aft and side-side fatigue damage as a function of wind/wave-misalignment $\psi$.

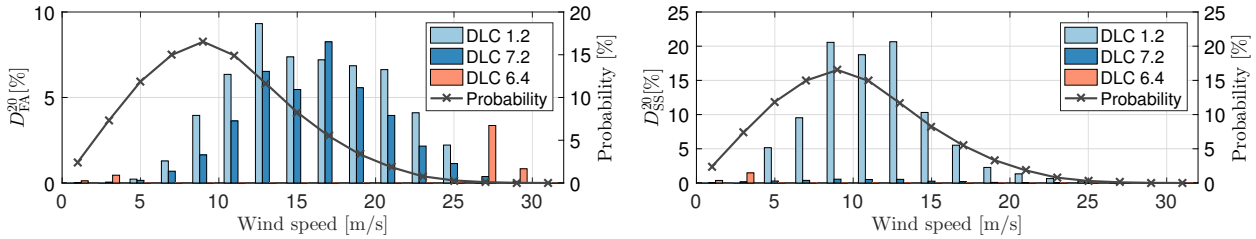


(a) Fore-aft direction.

(b) Side-side direction.

Figure 7: Lifetime probability and contribution to fore-aft and side-side fatigue damage as a function of wind speed $V$.

reduction of fore-aft vibrations also has a positive effect on the side-side vibrations, resulting in a reduction of the side-side fatigue damage as well. The fore-aft and side-side vibration modes have closely spaced natural frequencies, and coupling between the two modes is expected. Consequently, vibrational energy is transferred from the higher damped

mode (fore-aft) to the lower damped mode (side-side) [8]. Absorbing energy from the fore-aft mode therefore results in less energy being transferred to the side-side mode. Further, the blade root fatigue loads are also reduced as a result of AAD. Support structure vibrations cause inertia loads in the blade roots, which consequently are reduced by AAD. The reduction of inertia loads is seen to outweigh the increase in aerodynamic fatigue loads caused by the additional pitch activity. As expected, the increased pitch activity results in a considerable increase in both the pitch actuator fatigue loads, and the pitch actuator duty cycle. The shaft is also seen to be negatively affected by AAD, presumably due to increased variations in the shaft speed, and variations in the aerodynamic torque transferred to the low-speed end of the shaft.

AGT causes a considerable reduction of the side-side fatigue damage. Because the maximum fatigue damage is mainly caused by fatigue loads in the fore-aft direction, the improvement in $D^{20}_{\text{Max}}$ is moderate. Similar to AAD, the edgewise fatigue loads in the blade root are reduced as a consequence of the alleviation of inertia loads. Other undesirable side-effects of AGT is increased fatigue loads in the shaft, and increased variability of the power output. The results with AAD and AGT acting simultaneously show that the effect of the combined controllers cannot be determined accurately by considering the control strategies separately. However, for qualitative assessment of the controller performance, for example in the context of controller tuning or selection of environmental trigger criteria for the control strategies, it is acceptable to assume that the controllers are independent.

The gain of operating the wind turbine in wind speeds above the nominal cut-out wind speed (SCO) is small with respect to the maximum fatigue damage. Comparing the 2.9% improvement in $D^{20}_{\text{Max}}$ with the 0.11 % probability of wind speeds exceeding 26 [m/s], there is a clear advantage of SCO. Due to the low probability, the other performance parameters, including the lifetime energy yield, are not much affected by SCO. This conclusion is, however, dependent on the environmental conditions.

With AIC, a considerable improvement in both the fore-aft and maximum fatigue damage is achieved at the cost of only marginal side-effects. Similar to SCO, the gain in terms of $D^{20}_{\text{Max}}$ is significant when considering the 7.5 % probability of AIC being used. Because the generator is not operational, the drive-train is not strongly affected by AIC. However, a small increase in shaft fatigue loads is introduced by the additional aerodynamic torque. A slight increase in the side-side fatigue damage and edgewise blade root fatigue loads is also seen due to the reduced aeroelastic damping of the side-side vibration mode compared with the normal idling state. The aerodynamic loading of the blades is increased by AIC. However, similar to the case with AAD, the reduction of inertia loads outweighs the increased aerodynamic loads.

The fatigue loads in the gear ($\text{DEL}^{20}_{\text{Gear}}$), and the energy yield are not strongly affected by any of the control strategies. Gear fatigue is governed by the magnitude of the drive-train loading, and rotational speed, which are not much affected by the different control strategies. Furthermore, the control strategies that are enabled during power production cause only fluctuations in parameters that affect the energy yield, while the mean values remain approximately unchanged.

Table 4: . Lifetime comparison of load mitigation strategies with performance parameters given in percentage [%] of the baseline case. Favorable effects are indicated by green cells, and undesirable effects are indicated by red cells.

| | Support structure | | | Blade root | | Pitch actuators | | Drive-train | | Power production | |
|---|---|---|---|---|---|---|---|---|---|---|---|
| | $D^{20}_{\text{Max}}$ | $D^{20}_{\text{FA}}$ | $D^{20}_{\text{SS}}$ | $\text{DEL}^{20}_{\text{Edge}}$ | $\text{DEL}^{20}_{\text{Flap}}$ | $\text{DEL}^{20}_{\beta}$ | $\text{ADC}^{20}_{\beta}$ | $\text{DEL}^{20}_{\text{Gear}}$ | $\text{DEL}^{20}_{\text{Shaft}}$ | $P^{20}_{\text{Out}}$ | $P^{20}_{\text{Std}}$ |
| AAD | -27.8 | -27.6 | -8.9 | -5.0 | -4.6 | +30.8 | +192.8 | +0.3 | +9.2 | 0.0 | +0.2 |
| AGT | -9.1 | -0.4 | -60.1 | -22.1 | -1.2 | -0.7 | -2.8 | +0.1 | +2.4 | 0.0 | +4.0 |
| AAD/AGT | -34.0 | -27.4 | -63.5 | -22.5 | -4.6 | +30.8 | +193.8 | +0.4 | +11.2 | 0.0 | +2.8 |
| SCO | -2.9 | -3.0 | +0.1 | 0.0 | -0.3 | 0.0 | +0.2 | 0.0 | +0.8 | +0.1 | 0.0 |
| AIC | -17.9 | -23.5 | +2.8 | +0.1 | -1.4 | 0.0 | 0.0 | 0.0 | +1.1 | 0.0 | 0.0 |
| All | -52.4 | -51.3 | -60.7 | -21.4 | -6.7 | +30.8 | +194.0 | +0.4 | +12.4 | +0.1 | +3.8 |

### 4.3. Qualitative comparison with a 5MW offshore wind turbine

In the following, the results for the 10MW OWT in 30 meter water depth are compared with the results for the 5MW monopile OWT in 20 meter water depth studied in [7]. There are several important differences between these cases. Firstly, due to the larger monopile diameter and larger water depth, the 10MW OWT is subject to higher hydrodynamic loads. Moreover, the first modal period of the 5MW OWT is approximately 3.6 s, which is considerably farther away from typical wave periods compared with the 4.7 s modal period for the 10MW OWT. Finally, the 10MW OWT is equipped with a TMD, which reduces the fatigue load contribution from idling, and from side-side vibrations during normal operation. Details regarding implementation of the control strategies, such as controller gains, are in general different for the two cases. Furthermore, while a bi-linear S-N curve with exponents 3 and 5 is used for the 10MW OWT, a linear S-N curve with exponent 4 is used for the 5MW OWT. The present comparison should therefore be regarded as qualitative.

The fatigue damage reduction with all the considered control strategies combined is approximately 10% higher for the 10MW OWT. This difference is mainly related to AAD and AIC. With AAD, this is expected since the 5MW OWT is less susceptible to wave loads. Despite the absence of a TMD, the effect of AIC is reduced for the 5MW OWT, also partly as a consequence of the difference in hydrodynamic response amplitudes. There are some differences in how AIC is implemented between the two OWTs. For the 5MW OWT, the use of AIC is limited to wind speeds below 14 [m/s], and it is assumed independent of the type of fault. Moreover, for the 5MW OWT the pitch angle is adjusted as a function of the mean wind speed to maintain an approximately constant rotor speed during AIC. Due to the absence of a TMD, AGT control is more effective for the 5MW OWT. The same trend is seen for SCO, which is also affected by the higher probability of exceeding the cut-out wind speed for the design location considered for the 5MW OWT.

Comparable controller performance parameters are blade root fatigue loads, energy yield, and standard deviation of the power output. Unlike the 10MW OWT, the blade root edgewise fatigue loads are increased as a consequence of the control activity for the 5MW OWT. A similar trend is observed for the flapwise fatigue loads. The change in energy yield is similar for the two OWTs, except for the additional power production resulting from SCO, which is larger for the 5MW OWT. Finally, the increase in the standard deviation of the power output is considerably higher for the 5MW OWT. The 10MW OWT is equipped with a medium-speed generator, whereas the 5MW OWT is equipped with a smaller high-speed generator. The relative magnitudes of the fluctuation in the generator torque resulting from AGT are therefore larger for the 5MW OWT. Moreover, due the absence of the TMD, the side-side hydrodynamic response amplitudes are larger for the 5MW OWT.

### 4.4. Event-based use of control strategies

The desired level of fatigue load reduction can be achieved by limiting the use of control strategies to certain predefined situations, with activation of control strategies based on information about environmental conditions. Activation criteria should be derived in a rational manner with the aim of maximizing the fatigue load reduction, while limiting the undesired side-effects. It is assumed that the load mitigation strategies for idling situations are either adopted, or not used at all, such that situational use of operational controls are the only source of fatigue design flexibility. The trade-off between fatigue damage in the support structure and different performance parameters are given in Fig. 8 for all possible combinations of activation and deactivation criteria based on wind speed. The AAD controller and AGT controller are considered separately, and only the performance parameters that are significantly affected by the operational controls are investigated. No logic for switching is implemented in the simulations, and the results are computed as part of the post-processing. For example, if AAD control is used in wind speeds $V$ above a threshold $V_{\mathrm{Lim}}$, the result with baseline control for $V < V_{\mathrm{Lim}}$ is combined with the results with AAD control for $V \geq V_{\mathrm{Lim}}$.

The trade-off between fatigue damage in the fore-aft direction and the fatigue loads in the pitch actuators and the drive-train shaft is given in Fig. 8a for the AAD controller. Minimizing the wear of pitch actuators is the main priority when selecting activation criteria for AAD, however, it is desirable also to reduce the drive-train fatigue loads. The Pareto-optimal scenarios for $\mathrm{DEL}_{\beta}^{20}$ are far from optimal for $\mathrm{DEL}_{\mathrm{Shaft}}^{20}$, and vice versa. The scenarios with a single activation criterion on wind speed $V_{\mathrm{AAD}} \geq V_{\mathrm{Lim}}$ uncover some of the fundamental factors behind the results. Notably, whereas these points are all located at the Pareto-front for $\mathrm{DEL}_{\beta}^{20}$, they are some of the least optimal scenarios for $\mathrm{DEL}_{\mathrm{Shaft}}^{20}$. It is beneficial to limit the use of AAD in wind speeds below the rated wind speed, where the rotor is normally operated with constant pitch. The opposite trend is seen for the shaft fatigue loads, which are mainly affected by AAD when rated aerodynamic torque is reached. Although they are not presented in the plot, activation criteria of

the type $V_{\mathrm{ADD}} \leq V_{\mathrm{Lim}}$ are close to optimal for the shaft fatigue loads. The results for $\mathrm{ADC}_{\beta}^{20}$ are very similar to the result for $\mathrm{DEL}_{\beta}^{20}$, and they are therefore not presented.

The trade-offs associated with the AGT control action are presented in Fig. 8b. The trends observed for AGT are different to those of AAD. With the baseline controller, the standard deviation of both generator torque and the power output is most significant for wind speed below the rated wind speed where the rotor is operated with variable speed. The additional penalty of using AGT in terms of power output variability is therefore lower in the variable speed region. Moreover, the AGT control actions are only significant when there is a sufficient amount of sideways excitation from wave loads. This is supported by the labeled scenarios, showing that with regard to fluctuations in the power output, it is desirable to limit the use of AGT in high wind speeds. The Pareto-optimal activation criteria for $P_{\mathrm{Std}}^{20}$ are in some cases also close to optimal for $\mathrm{DEL}_{\mathrm{Shaft}}^{20}$. The same is not true for the Pareto-optimal scenarios for $\mathrm{DEL}_{\mathrm{Shaft}}^{20}$, which are scattered all over the plot for $P_{\mathrm{Std}}^{20}$. The scenarios with a single activation criterion on wind speed $V_{\mathrm{AGT}} \leq V_{\mathrm{Lim}}$ (opposite to $V_{\mathrm{AAD}}$), are all close to or on the Pareto-front for $P_{\mathrm{STD}}^{20}$, and in some cases also close to optimal for $\mathrm{DEL}_{\mathrm{Shaft}}^{20}$.

For both AAD and the AGT control, it is concluded that the most important side-effects are governed by the mode of the control system, rather than the source of the fatigue loads. Furthermore, if wear of pitch actuators and variability of the power output is the main concern, a single activation/deactivation criterion on wind speed is sufficient.

### *4.5. Varying site conditions*

Finally, the possibility of using load mitigation strategies to compensate for site variability is investigated. Two types of variability in site conditions are investigated; these are variability in water depth, and variability in soil conditions affecting the soil stiffness. Only site-specific variations which affect the modal properties of the OWT are considered. Site-specific variations in environmental conditions such as wake effects, turbulence intensity, and sea states, are not considered. The only change applied to the wind turbine under the varying site conditions, is tuning of the TMD to the modified first natural frequency of the support structure. When the variation in water depth is considered, the monopile length is kept unchanged, and the water depth is scaled with a factor $\eta_{\mathrm{Depth}}$. The monopile penetration depth is adjusted to compensate for the change in water depth, meaning that if, for example, the water depth is increased with 3 meters, the monopile penetration depth is reduced with 3 meters. The monopile penetration depth is primarily determined based on ULS considerations. The aim of the present analysis is to analyse the effect of variations in site conditions for a given foundation design. It is assumed that the change in water depth is within a range which does not require modification of the monopile penetration depth. When variation in soil conditions is considered, the soil profile is kept unchanged, and the soil stiffness is scaled with a factor $\eta_{\mathrm{Soil}}$. The modal damping ratios are affected by changes in the modal characteristics resulting from the variations in site conditions. The damping properties of the support structure are not modified to compensate for the variation in damping ratios.

The 20-year maximum fatigue damage over the circumference of the foundation with the baseline OWT controller is presented in Fig. 9 as a function of $\eta_{\mathrm{Soil}}$ and $\eta_{\mathrm{Depth}}$. The results are normalized with the baseline case ($\eta_{\mathrm{Soil}} = \eta_{\mathrm{Depth}} = 1.0$). Furthermore, the corresponding variation in the the first modal frequency, and the damping ratio is given in Fig. 10. Because the first modal frequencies in the fore-aft and side-side direction are in close proximity, only the fore-aft frequency is presented. Variation in the soil conditions affects the mode shapes and natural frequencies of the support structure. Increased stiffness and damping leads to reduced vibration amplitudes with less fatigue damage as a result, and vice versa. Moreover, the natural frequency is shifted closer to, or further away, from typical wave frequencies, altering the dynamic response to wave loads. Due to the large difference in damping between operation and idling, the changes in modal characteristics affect DLC 7.2 more than DLC 1.2. For this reason, the relative contribution to the lifetime fatigue damage from DLC 7.2 increase as the stiffness- and damping-contribution from the soil is reduced. The results for variation in water depth are similar to the results for soil variations, however, the monopile fatigue damage is seen to be even more sensitive to variations in the water depth. When the monopile penetration depth is changed, the modal characteristics are altered, affecting the natural frequencies and response amplitudes. In addition, the magnitude of the hydrodynamic loads depends on the water depth, which adds to the sensitivity of fatigue loads to variations in the water depth.

Four different scenarios of variation in site conditions around the baseline design case are investigated in the context of control strategies for fatigue load reduction. Each scenario consists of two sub-cases, denoted as the reference case and the controlled case. The reference case is the site condition with the least amount of monopile fatigue damage

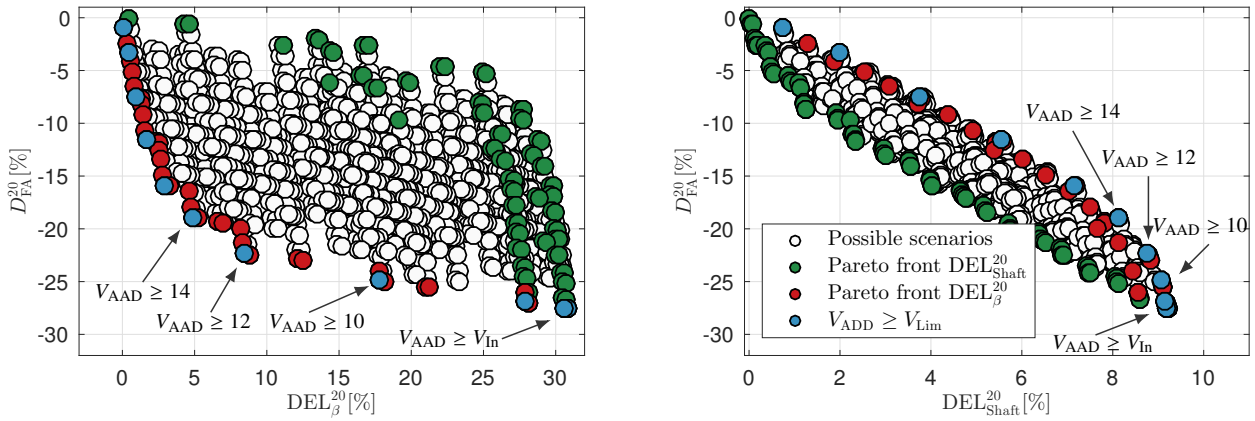


(a) System trade-offs for the AAD controller. $V_{\mathrm{AAD}} \geq V_{\mathrm{Lim}}$ means that the AAD controller is enabled for all wind speeds above $V_{\mathrm{Lim}}$.

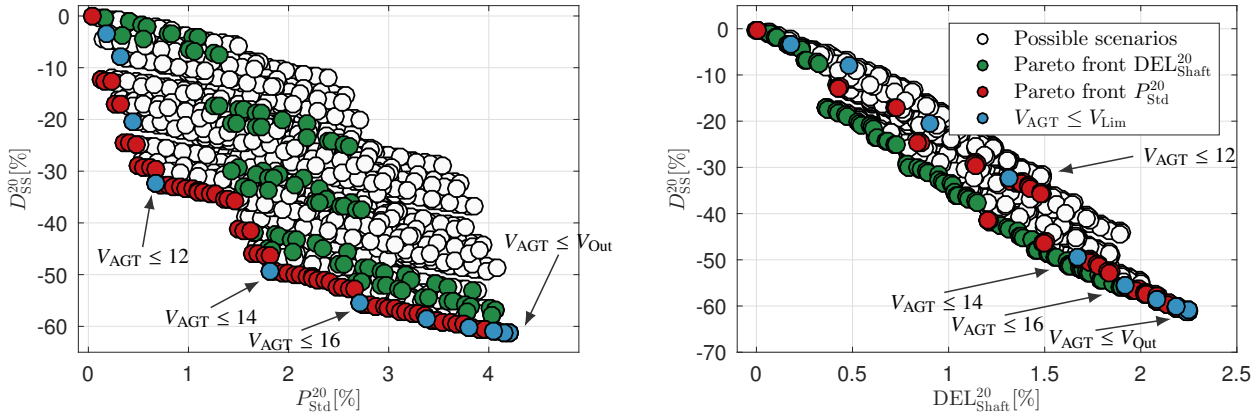


(b) System trade-offs for the AGT controller. $V_{\mathrm{AGT}} \leq V_{\mathrm{Lim}}$ means that the AGT controller is enabled for all wind speeds below $V_{\mathrm{Lim}}$.

Figure 8: Trade-offs between fatigue load reduction and undesirable side-effects for the AAD and AGT controller. All the possible trade-off scenarios with different trigger criteria on wind speed are presented. The Pareto-optimal scenarios for the investigated parameters are indicated by colored spots. The results show that if wear of pitch actuators and variability of the power output is the main concern, a single activation/deactivation criterion on wind speed is Pareto-optimal.

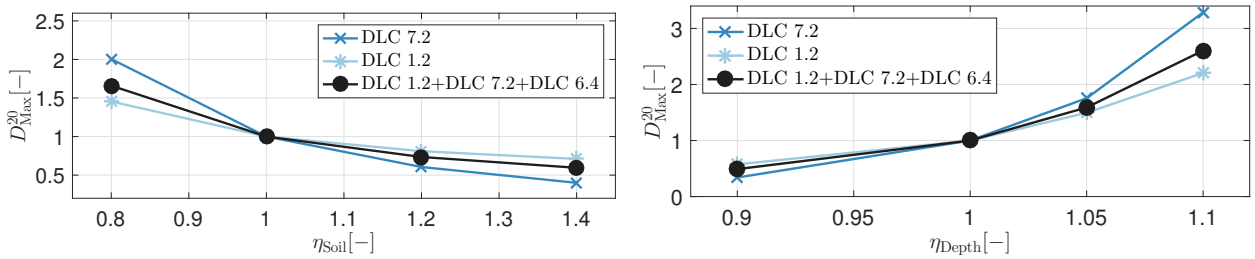


(a) Soil condtions.

(b) Water depth.

Figure 9: Normalized maximum fatigue damage over the circumference of the foundation under varying site conditions. Results are presented for the critical cross-section 6 meters below the mudline.

out of the two sub-cases, and the controlled case is the site condition for which the control strategies for fatigue load reduction is applied. The operational controls considered are AAD and AGT, and the use of these control strategies is restricted to the boundaries on the wind speed given in Table 5. These boundaries are chosen based on the previously

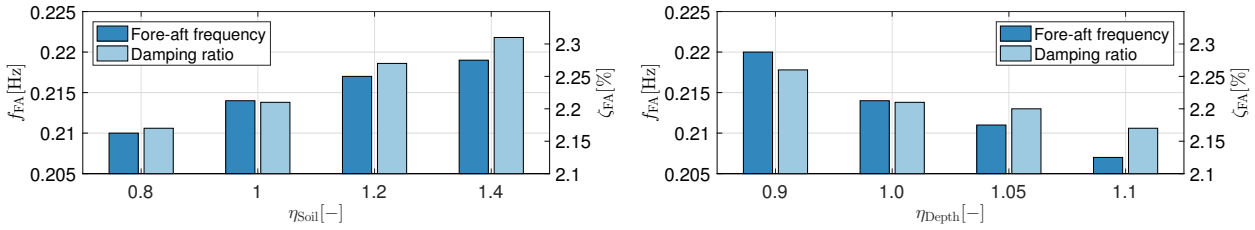


(a) Soil condtions.

(b) Water depth.

Figure 10: Variations in the fore-aft modal frequency $f_{FA}$ and the fore-aft damping ratio $\zeta_{FA}$ under varying site conditions.

presented results, assuming that the side-effects of primary interest are pitch actuator wear, and the standard devation of power output. Furthermore, the idling controllers AIC and SCO are applied for both the reference cases and the controlled cases to reduce the impact of DLC 6.4 and DLC 7.2.

First, the effect of variations in site conditions on the performance of the control strategies is investigated. Identical to the analysis performed in Sec. 4.2, the lifetime effect of permanently enabled control strategies is presented for $\eta_{soil} = 0.8$, and $\eta_{soil} = 1.05$ in Appendix A. In both cases the global stiffness and damping are reduced compared with the baseline case, resulting in higher response amplitudes, and increased effectiveness of AGT and AIC. The cost is a moderate increase in collateral effects, particularly for the AGT controller. The AAD control activity is only marginally affected by the changes in site conditions. However, the influence of AAD on the lifetime accumulated fatigue damage is reduced as a consequence of the increased importance of idling situations.

The monopile fatigue damage in the four scenarios is given in Fig. 11, and the effect on the other system parameters is presented in Table 6. In all scenarios, except scenario IV, the combination of AAD and AGT is capable of compensating for the variation in site conditions, at the cost of only moderate side-effects. The 3 meter change in water depth demonstrated by Scenario IV, is only partly counteracted by the operational controls, and the pitch actuators are severely affected by the control action compared with the other scenarios. The ability of the operational controls to compensate for variations in the site conditions depends on the global stiffness and damping. Comparing, for example, scenario I with scenario II, the difference in support structure fatigue damage resulting from the change in soil stiffness is lower for scenario II. Consequently, the adverse side-effects to the pitch actuators are less severe for scenario II. The same trend is observed for variations in the water depth.

Table 5: Four scenarios for variations in site conditions compesated by use of control strategies for fatigue load reduction. $\mathcal{S}_{AAD}$ and $\mathcal{S}_{AGT}$ are the sets of wind speeds for which AAD control and AGT control is enabled, and $\mathcal{V}$ is the set of all wind speeds.

| Scenario | Type of variability | Reference case | Controlled case | $\mathcal{S}_{AAD}$ | $\mathcal{S}_{AGT}$ |
|---|---|---|---|---|---|
| I | Soil | $\eta_{Soil} = 1.0$ | $\eta_{Soil} = 0.8$ | $\{V \in \mathcal{V} : V_{Out} > V > 12\}$ | $\{V \in \mathcal{V} : 14 > V > V_{In}\}$ |
| II | Soil | $\eta_{Soil} = 1.2$ | $\eta_{Soil} = 1.0$ | $\{V \in \mathcal{V} : V_{Out} > V > 16\}$ | $\{V \in \mathcal{V} : 14 > V > V_{In}\}$ |
| III | Depth | $\eta_{Depth} = 1.0$ | $\eta_{Depth} = 1.05$ | $\{V \in \mathcal{V} : V_{Out} > V > 12\}$ | $\{V \in \mathcal{V} : 16 > V > V_{In}\}$ |
| IV | Depth | $\eta_{Depth} = 0.9$ | $\eta_{Depth} = 1.0$ | $\{V \in \mathcal{V} : V_{Out} > V > 10\}$ | $\{V \in \mathcal{V} : 16 > V > V_{In}\}$ |

## 5. Conclusions

The present work analysed the applicability of control system design to compensate for differing fatigue loads in the support structure due to varying site conditions. The design case was a 10MW offshore wind turbine in 30 meters water depth at the Dogger Bank in the North Sea. Long-term variations in environmental conditions given by 60-years of hindcast data for the design location were combined with short-term aero-hydro-servo elastic simulations in the 20-year assessment of the fatigue strength for the support structure. Control strategies applicable for both normal operation and idling situations were considered. The operational control strategies included active aerodynamic

Table 6: Lifetime comparison of the controlled case with the reference case for scenario I-IV. The results are given in percentage [%] of reference case.

| | Support structure | | | Blade root | | Pitch actuator | | Drive-train | | Power production | |
|---|---|---|---|---|---|---|---|---|---|---|---|
| Scenario | $D^{20}_{\text{Max}}$ | $D^{20}_{\text{FA}}$ | $D^{20}_{\text{SS}}$ | $\text{DEL}^{20}_{\text{Edge}}$ | $\text{DEL}^{20}_{\text{Flap}}$ | $\text{DEL}^{20}_{\beta}$ | $\text{ADC}^{20}_{\beta}$ | $\text{DEL}^{20}_{\text{Gear}}$ | $\text{DEL}^{20}_{\text{Shaft}}$ | $P^{20}_{\text{Out}}$ | $P^{20}_{\text{STD}}$ |
| I | +0.5 | +0.3 | +4.3 | +7.7 | +2.4 | +10.4 | +43.1 | +0.4 | +10.6 | 0.0 | +2.2 |
| II | -3.6 | -2.6 | -12.7 | +1.4 | -0.1 | +3.2 | +17.6 | +0.3 | +8.5 | 0.0 | +1.7 |
| III | -1.1 | -2.5 | +2.8 | +6.5 | -1.4 | +9.6 | +41.0 | +0.4 | +10.8 | 0.0 | +3.1 |
| IV | +16.9 | +15.0 | +26.0 | +1.0 | -0.2 | +18.9 | +63.5 | +0.4 | +10.5 | 0.0 | +2.4 |

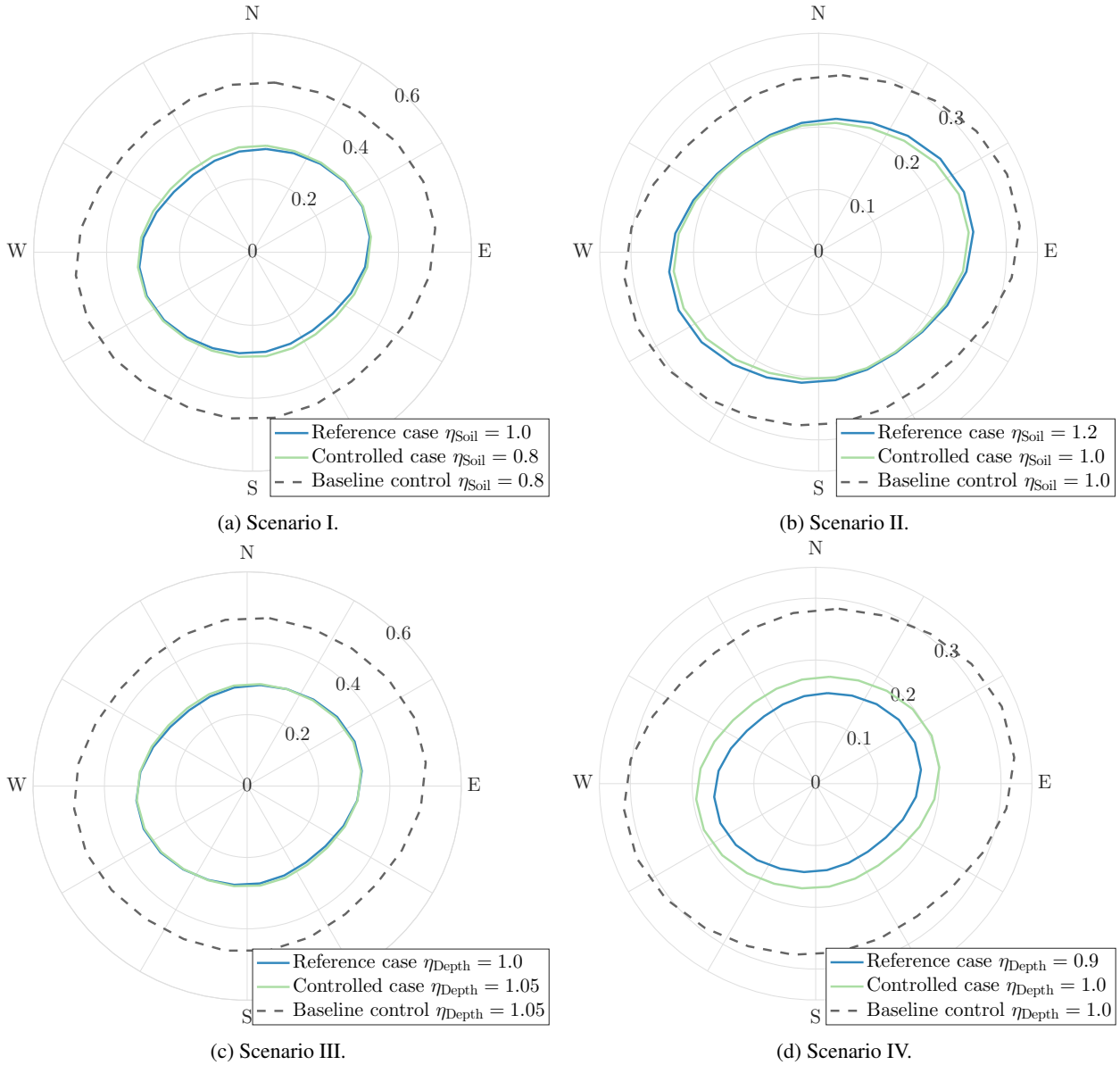


(a) Scenario I.

(b) Scenario II.

(c) Scenario III.

(d) Scenario IV.

Figure 11: Radial distribution of fatigue damage in the foundation for scenario I-IV.

damping control for reduction of fatigue loads in the fore-aft direction, and active generator torque control for reduction of fatigue loads in the side-side direction. The idling control strategies included active idling control and soft cut-out control, both primarily for reduction of fatigue loads in the fore-aft direction.

For the baseline design case, the fatigue damage was nonuniformly distributed around the circumference of the support structure, with southwest/northeast being the most critical orientations. This corresponded with the primary direction of wind and wind-sea, which for the design location is southwest. Approximately 20% of the total fatigue damage was caused by wave loads acting in the side-side direction, and despite only 10% unavailability, this design situation contributed with approximately 35% of the total fatigue damage. Further, the performance of the control strategies in terms of fatigue load reduction, and effect on other wind turbine components, was analysed. Results showed that a total fatigue load reduction of approximately 50% was possible, at the cost of increased wear of pitch actuators, increased fatigue loads in the drive-train shaft, and increased fluctuations in the power output. Other system parameters were only moderately affected. Undesirable side-effects may be significantly reduced by limiting the use of the operational control strategies to some predefined situations. Particularly, the wear of pitch actuators due to active aerodynamic damping, was reduced by approximately 50% by restricting the use of this control strategy to wind speeds above the rated wind speed. It was also shown that the fluctuations in power output could be reduced by limiting the use of active generator torque control in high wind speeds.

Two types of variability in the site conditions were investigated: variations in soil conditions affecting the soil stiffness, and variations in the water depth. The fatigue loads in the support structure were more sensitive to variations in the water depth than to variations in the soil conditions. Furthermore, due to the large difference in system damping between operation and idling, the relative contribution to fatigue damage from idling conditions increased with decreasing soil stiffness. Further, the operational control strategies were used to compensate for the changes in fatigue loads arising from the variations in site conditions. With only moderate cost to other system components, the control system was able to compensate for a 20% variation in soil stiffness. Similar results were achieved with a 5% (1.5 meters) increase in water depth. The control system was not fully capable of compensating for a 10% increase in water depth from 27 meters to 30 meters, and the undesirable side-effects were more severe compared with the other scenarios.

The results indicated that the wind turbine's control system is uselful for compensating for variations in the soil conditions. The results with respect to water depth were less promising. There is a clear advantage of the presented methodology in terms of reducing the design conservatism associated with foundation clustering including also variations in water depth. However, limiting the scope to soil variability, and including also uncertainty in soil parameters, is likely a more suitable application. The adverse side-effects associated with the presented methodology were not insignificant. Control strategies and methodology to further improve the trade-off between support structure fatigue damage and adverse side-effects should be developed. Active aerodynamic damping had the most severe side-effects. For large OWTs in moderate water depth, such as the present design case, severe sea states represent a considerable contribution to the lifetime accumulated fatigue damage. In severe sea states, the wave induced motion is dominated by the quasi-static response, which is governed by the global stiffness. Active pitch control to increase both the damping and stiffness of the fore-aft vibration modes is therefore a strategy which should be explored. Finally, considering the large potential for fatigue load reduction with active idling control, the literature on this control strategy is sparse. Further research on active idling control is recommended.

## Acknowledgments

This work has been carried out at the Centre for Autonomous Marine Operations and Systems (NTNU AMOS). The Norwegian Research Council is acknowledged as the main sponsor of NTNU AMOS. This work was supported by the Research Council of Norway through the Centres of Excellence funding scheme, Project number 223254 - NTNU AMOS. The authors would also like to thank Dr. Amir R. Nejad for his invaluable assistance on aspects regarding drive-train fatigue calculations.

## Appendix A. Control Strategy Comparison Under Varying Site Conditions

Table A.7: . Lifetime comparison of load mitigation strategies with performance parameters given in percentage [%] of the baseline control case with $\eta_{\text{Soil}} = 0.8$.

| | Support structure | | | Blade root | | Pitch actuator | | Drive-train | | Power production | |
|---|---|---|---|---|---|---|---|---|---|---|---|
| | $D^{20}_{\text{Max}}$ | $D^{20}_{\text{FA}}$ | $D^{20}_{\text{SS}}$ | $\text{DEL}^{20}_{\text{Edge}}$ | $\text{DEL}^{20}_{\text{Flap}}$ | $\text{DEL}^{20}_{\beta}$ | $\text{ADC}^{20}_{\beta}$ | $\text{DEL}^{20}_{\text{Gear}}$ | $\text{DEL}^{20}_{\text{Shaft}}$ | $P^{20}_{\text{Out}}$ | $P^{20}_{\text{Std}}$ |
| AAD | -25.6 | -25.5 | -5.7 | -2.4 | -2.2 | +33.0 | +202.2 | +0.3 | +9.2 | 0.0 | +0.2 |
| AGT | -10.8 | -0.4 | -61.9 | -23.7 | -1.0 | -0.7 | -2.7 | +0.2 | +3.1 | 0.0 | +4.9 |
| AAD/AGT | -33.7 | -25.4 | -65.4 | -23.0 | -2.1 | +32.9 | +203.3 | +0.4 | +11.8 | 0.0 | +4.6 |
| SCO | -3.8 | -3.9 | +0.1 | 0.0 | -7.7 | +0.0 | +0.2 | 0.0 | +0.8 | +0.1 | 0.0 |
| AIC | -23.4 | -31.1 | +2.0 | +0.1 | -10.7 | 0.0 | 0.0 | +0.0 | +1.1 | 0.0 | 0.0 |
| All | -57.4 | -56.9 | -63.4 | -22.3 | -15.4 | +32.9 | +203.5 | +0.5 | +13.0 | +0.1 | +4.6 |

Table A.8: . Lifetime comparison of load mitigation strategies with performance parameters given in percentage [%] of the baseline control case with $\eta_{\text{Depth}} = 1.05$.

| | Support structure | | | Blade root | | Pitch actuator | | Drive-train | | Power production | |
|---|---|---|---|---|---|---|---|---|---|---|---|
| | $D^{20}_{\text{Max}}$ | $D^{20}_{\text{FA}}$ | $D^{20}_{\text{SS}}$ | $\text{DEL}^{20}_{\text{Edge}}$ | $\text{DEL}^{20}_{\text{Flap}}$ | $\text{DEL}^{20}_{\beta}$ | $\text{ADC}^{20}_{\beta}$ | $\text{DEL}^{20}_{\text{Gear}}$ | $\text{DEL}^{20}_{\text{Shaft}}$ | $P^{20}_{\text{Out}}$ | $P^{20}_{\text{Std}}$ |
| AAD | -25.8 | -26.3 | -5.0 | -1.5 | -3.9 | +32.0 | +198.1 | +0.3 | +9.2 | 0.0 | +0.2 |
| AGT | -12.0 | -0.5 | -62.0 | -23.4 | -1.3 | -0.7 | -2.6 | +0.2 | +3.2 | 0.0 | +4.9 |
| AAD/AGT | -34.9 | -26.2 | -65.2 | -22.5 | -4.0 | +31.9 | +199.2 | +0.4 | +11.9 | 0.0 | +4.7 |
| SCO | -3.1 | -3.3 | +0.1 | 0.0 | -0.8 | 0.0 | +0.2 | 0.0 | +0.8 | +0.1 | 0.0 |
| AIC | -17.3 | -24.9 | +1.9 | +0.1 | -1.6 | 0.0 | 0.0 | 0.0 | +0.7 | 0.0 | 0.0 |
| All | -55.4 | -54.5 | -63.2 | -21.7 | -7.9 | +31.9 | +199.4 | +0.5 | +13.1 | +0.1 | +4.7 |

## Appendix B. Environmental Load Cases

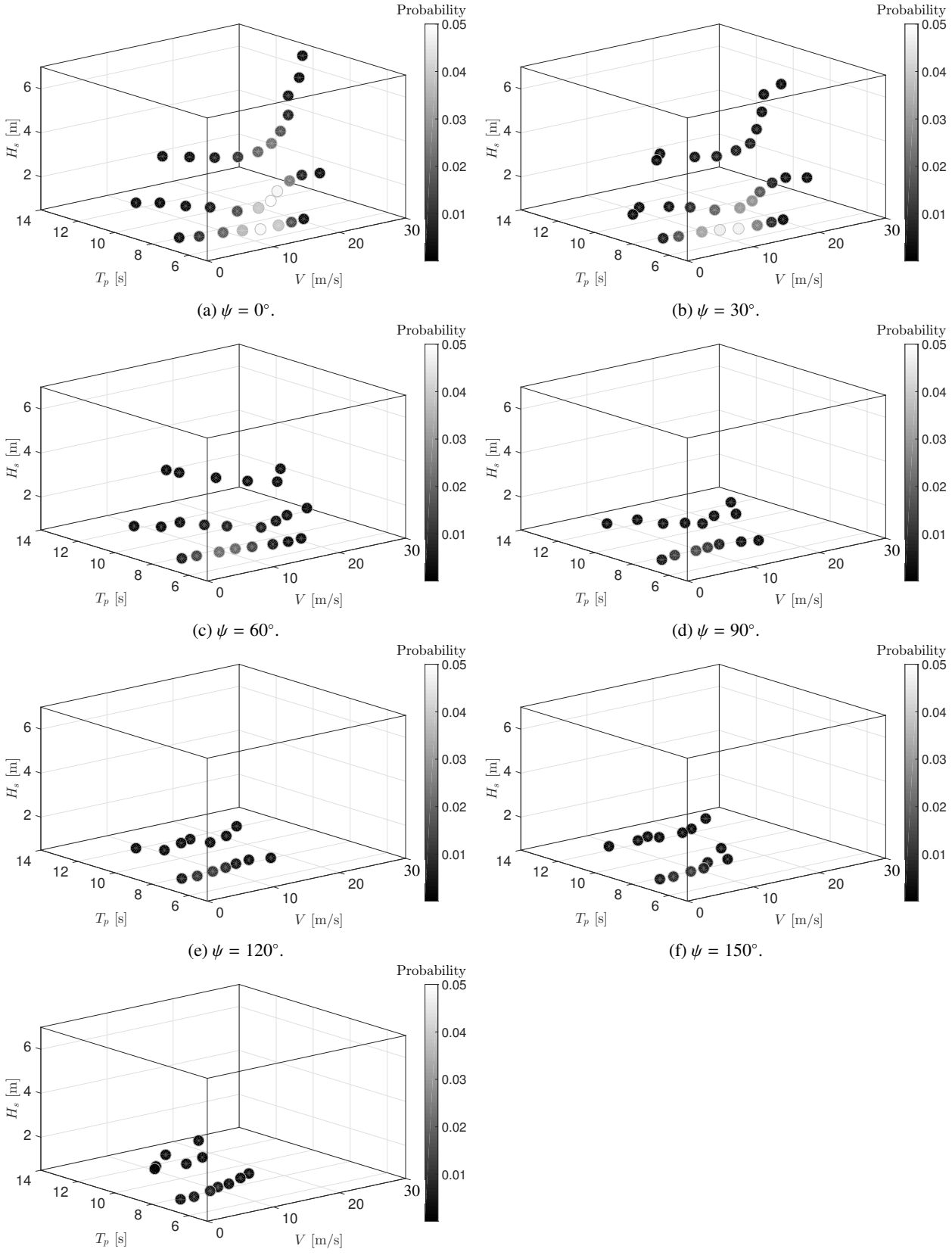


(a) $\psi = 0°$.

(b) $\psi = 30°$.

(c) $\psi = 60°$.

(d) $\psi = 90°$.

(e) $\psi = 120°$.

(f) $\psi = 150°$.

(g) $\psi = 180°$.

Figure B.12: Environmental load cases (ELC) for each group of wind/wave misalignment $\psi$.

## References


[1] A. Ho, A. Mbistrova, G. Corbetta, I. Pineda, K. Ruby, The european offshore wind industry-key trends and statistics 2016, Report. Brussels: European Wind Energy Association.

[2] P. Gardner, A. Garrad, P. Jamieson, H. Snodin, A. Tindal, Wind energy–the facts, Technology, Part I.

[3] B. Shrestha, M. Kühn, Tailoring the employment of offshore wind turbine support structure load mitigation controllers, in: Journal of Physics: Conference Series, Vol. 753, IOP Publishing, 2016, p. 052032.

[4] E. E. Bachynski, H. Ormberg, Hydrodynamic modeling of large-diameter bottom-fixed offshore wind turbines, in: ASME 2015 34th International Conference on Ocean, Offshore and Arctic Engineering, American Society of Mechanical Engineers, 2015, p. V009T09A051.

[5] T. Fischer, W. Vries, P. Rainey, B. Schmidt, K. Argyriadis, M. Kühn, Offshore support structure optimization by means of integrated design and controls, Wind Energy 15 (1) (2012) 99–117.

[6] E. Smilden, E. E. Bachynski, A. J. Sørensen, Key contributors to lifetime accumulated fatigue damage in an offshore wind turbine support structure, in: ASME 2017 36th International Conference on Ocean, Offshore and Arctic Engineering, American Society of Mechanical Engineers, 2017, p. V010T09A075.

[7] T. A. Fischer, Mitigation of aerodynamic and hydrodynamic induced loads of offshore wind turbines, Shaker, 2012, University of Stuttgart.

[8] M. Damgaard, L. B. Ibsen, L. V. Andersen, J. K. Andersen, Cross-wind modal properties of offshore wind turbines identified by full scale testing, Journal of Wind Engineering and Industrial Aerodynamics 116 (2013) 94–108.

[9] C. Devriendt, P. J. Jordaens, G. De Sitter, P. Guillaume, Damping estimation of an offshore wind turbine on a monopile foundation, IET Renewable Power Generation 7 (4) (2013) 401–412.

[10] R. Shirzadeh, C. Devriendt, M. A. Bidakhvidi, P. Guillaume, Experimental and computational damping estimation of an offshore wind turbine on a monopile foundation, Journal of Wind Engineering and Industrial Aerodynamics 120 (2013) 96–106.

[11] E. Van der Hooft, P. Schaak, T. Van Engelen, Wind turbine control algorithms, DOWEC project-DOWEC-F1W1-EH-03-094/0, Task-3 report.

[12] E. Bossanyi, Wind turbine control for load reduction, Wind energy 6 (3) (2003) 229–244.

[13] E. Bossanyi, G. Ramtharan, B. Savini, The importance of control in wind turbine design and loading, in: Control and Automation, 2009. MED'09. 17th Mediterranean Conference on, IEEE, 2009, pp. 1269–1274.

[14] B. Fischer, M. Shan, A survey on control methods for the mitigation of tower loads, Fraunhofer-Institute for Wind Energy and Energy Systems Technology, IWES Project report 01/104256.

[15] M. Shan, J. Jacobsen, S. Adelt, Field testing and practical aspects of load reducing pitch control systems for a 5 mw offshore wind turbine, Proc. EWEA (2013) 101–05.

[16] J. M. Trumars, J. O. Jonsson, L. Bergdahl, The effect of wind and wave misalignment on the response of a wind turbine at Bockstigen, in: 25th International Conference on Offshore Mechanics and Arctic Engineering, American Society of Mechanical Engineers, 2006, pp. 635–641.

[17] J.-T. H. Horn, J. Krokstad, J. Amdahl, Joint probability distribution of environmental conditions for design of offshore wind turbines, in: ASME 2017 36th International Conference on Ocean, Offshore and Arctic Engineering, American Society of Mechanical Engineers, 2017, p. V010T09A068.

[18] T. Fischer, P. Rainey, E. Bossanyi, M. Kühn, Study on control concepts suitable for mitigation of loads from misaligned wind and waves on offshore wind turbines supported on monopiles, Wind Engineering 35 (5) (2011) 561–573.

[19] Z. Zhang, S. R. Nielsen, F. Blaabjerg, D. Zhou, Dynamics and control of lateral tower vibrations in offshore wind turbines by means of active generator torque, Energies 7 (11) (2014) 7746–7772.

[20] L. Ziegler, S. Voormeeren, S. Schafhirt, M. Muskulus, Sensitivity of wave fatigue loads on offshore wind turbines under varying site conditions, Energy Procedia 80 (2015) 193–200.

[21] M. Damgaard, L. V. Andersen, L. B. Ibsen, Dynamic response sensitivity of an offshore wind turbine for varying subsoil conditions, Ocean Engineering 101 (2015) 227–234.

[22] S. Schafhirt, A. Page, G. R. Eiksund, M. Muskulus, Influence of soil parameters on the fatigue lifetime of offshore wind turbines with monopile support structure, Energy Procedia 94 (2016) 347–356.

[23] L. Ziegler, S. Voormeeren, S. Schafhirt, M. Muskulus, Design clustering of offshore wind turbines using probabilistic fatigue load estimation, Renewable Energy 91 (2016) 425–433.

[24] W. Carswell, S. R. Arwade, D. J. DeGroot, M. A. Lackner, Soil–structure reliability of offshore wind turbine monopile foundations, Wind Energy 18 (3) (2015) 483–498.

[25] M. Damgaard, L. V. Andersen, L. B. Ibsen, H. S. Toft, J. D. Sørensen, A probabilistic analysis of the dynamic response of monopile foundations: Soil variability and its consequences, Probabilistic Engineering Mechanics 41 (2015) 46–59.

[26] P. Tavner, Offshore wind turbines: Reliability, Availability and Maintenance, The Institution of Engineering and Technology, London, UK.

[27] M. Wilkinson, B. Hendriks, F. Spinato, K. Harman, E. Gomez, H. Bulacio, J. Roca, P. Tavner, Y. Feng, H. Long, Methodology and results of the reliawind reliability field study, in: European Wind Energy Conference and Exhibition 2010, EWEC 2010, Vol. 3, Sheffield, 2010, pp. 1984–2004.

[28] F. D. Bianchi, H. De Battista, R. J. Mantz, Wind turbine control systems: principles, modelling and gain scheduling design, Springer Science & Business Media, 2006.

[29] F. Perrone, M. Kühn, Offshore wind turbine tower fore-aft fatigue load reduction by coupling control and vibrational analysis, Journal of Ocean and Wind Energy 2 (3) (2015) 168–175.

[30] F. Perrone, Offshore wind turbine tower fore-aft control: Trade-off fatigue load reduction and pitch activity, in: Control Conference (ECC), 2015 European, IEEE, 2015, pp. 2444–2448.

[31] B. Shrestha, M. Kühn, Adaptation of controller concepts for support structure load mitigation of offshore wind turbines, Energy Procedia 94 (2016) 241–248.

[32] C. Bak, F. Zahle, R. Bitsche, T. Kim, A. Yde, L. Henriksen, A. Natarajan, M. Hansen, Description of the DTU 10 MW reference wind turbine, DTU Wind Energy Report-I-0092.

[33] M. Reistad, Ø. Breivik, H. Haakenstad, O. J. Aarnes, B. R. Furevik, J.-R. Bidlot, A high-resolution hindcast of wind and waves for the North Sea, the Norwegian Sea, and the Barents Sea, Journal of Geophysical Research: Oceans 116 (C5).
[34] P. A. Brodtkorb, P. Johannesson, G. Lindgren, I. Rychlik, J. Rydén, E. Sjö, et al., Wafo-a matlab toolbox for analysis of random waves and loads, in: The Tenth International Offshore and Polar Engineering Conference, International Society of Offshore and Polar Engineers, 2000.
[35] H. Markou, T. J. Larsen, Control strategies for operation of pitch regulated turbines above cut-out wind speeds, in: 2009 European Wind Energy Conference and Exhibition, 2009.
[36] M. H. Hansen, L. C. Henriksen, Basic DTU wind energy controller, Tech. rep., DTU Wind Energy (2013).
[37] W. Carswell, Soil-structure modeling and design considerations for offshore wind turbine monopile foundations.
[38] G. M. Stewart, M. A. Lackner, The impact of passive tuned mass dampers and wind–wave misalignment on offshore wind turbine loads, Engineering Structures 73 (2014) 54–61.
[39] DNV GL, Loads and site conditions for wind turbines, DNVGL-ST-0437.
[40] International Electrotechnical Commission (IEC), IEC 61400-1: Wind turbines part 1: Design requirements, Tech. rep. (2005).
[41] M. J. Kühn, Dynamics and design optimisation of offshore wind energy conversion systems, TU Delft, Delft University of Technology, 2001.
[42] DNV GL, DNV-RP-C205, Environmental conditions and environmental loads.
[43] B. J. Jonkman, Turbsim user's guide: Version 1.50.
[44] J. Carroll, A. McDonald, I. Dinwoodie, D. McMillan, M. Revie, I. Lazakis, Availability, operation and maintenance costs of offshore wind turbines with different drive train configurations, Wind Energy 20 (2) (2017) 361–378.
[45] API, RP, 2GEO (2011), Recommended Practice for Geotechnical Foundation Design Consideration.
[46] H. Ormberg, E. E. Bachynski, et al., Global analysis of floating wind turbines: Code development, model sensitivity and benchmark study, in: The Twenty-second International Offshore and Polar Engineering Conference, International Society of Offshore and Polar Engineers, 2012.
[47] O. Faltinsen, Sea loads on ships and offshore structures, Vol. 1, Cambridge university press, 1993.
[48] M. Matsuishi, T. Endo, Fatigue of metals subjected to varying stress, Japan Society of Mechanical Engineers, Fukuoka, Japan 68 (2) (1968) 37–40.
[49] DNV GL, Fatigue design of offshore steel structures, No. DNV-RP-C203.
[50] DNV GL, OS-C101, Design of Offshore Steel Structures, General (LRFD Method).
[51] G. Freebury, W. D. Musial, Determining equivalent damage loading for full-scale wind turbine blade fatigue tests, National Renewable Energy Laboratory Golden, CO, 2000.
[52] T. Burton, D. Sharpe, N. Jenkins, E. Bossanyi, Wind energy handbook, 2nd Edition, John Wiley & Sons, 2011.
[53] A. R. Nejad, Z. Gao, T. Moan, On long-term fatigue damage and reliability analysis of gears under wind loads in offshore wind turbine drivetrains, International Journal of Fatigue 61 (2014) 116–128.
[54] B. Niederstucke, A. Anders, P. Dalhoff, R. Grzybowski, Load data analysis for wind turbine gearboxes, Final Report of Enhanced Life Analysis of Wind Power Systems.
[55] C. Bottasso, F. Campagnolo, A. Croce, C. Tibaldi, Optimization-based study of bend–twist coupled rotor blades for passive and integrated passive/active load alleviation, Wind Energy 16 (8) (2013) 1149–1166.
[56] Standard, ISO, 6336–6 (2006) Calculation of load capacity of spur and helical gears Part 6: Calculation of service life under variable load, International Organization for Standardization, Geneva, Switzerland.
[57] Standard, ISO, 6336–3 (2006) Calculation of load capacity of spur and helical gears Part 6: Calculation of tooth bending stress, International Organization for Standardization, Geneva, Switzerland.
[58] K. A. Stol, W. Zhao, A. D. Wright, Individual blade pitch control for the controls advanced research turbine, Journal of solar energy engineering 128 (4) (2006) 498–505.
[59] C. Devriendt, P. Jordaens, G. Sitter, P. Guillaume, Damping estimation of an offshore wind turbine on a monopile foundation, IET Renewable Power Generation 7 (4) (2013) 401–412.
[60] M. H. Hansen, K. Thomsen, P. Fuglsang, T. Knudsen, Two methods for estimating aeroelastic damping of operational wind turbine modes from experiments, Wind Energy 9 (1-2) (2006) 179–191.